

Concerted Carrier-Barrier Dynamics in van der Waals Schottky Junctions Revealed by Time-Resolved Atomic Force Microscopy

Munenori Yokota^{1‡}, Hiroyuki Mogi^{2‡}, Yutaka Mera³, Katsuya Iwaya^{1*}, Taketoshi Minato^{4,5},
Shoji Yoshida², Osamu Takeuchi², Tatsuo Nakagawa¹, and Hidemi Shigekawa^{2*}

¹ UNISOKU Co., Ltd., Osaka 573-0131, Japan.

² Faculty of Pure and Applied Sciences, University of Tsukuba, Ibaraki 305-8573, Japan.

³ Department of Fundamental Biosciences (Physics), Shiga University of Medical Science, Shiga 520-2192, Japan.

⁴ Institute for Molecular Science (IMS), National Institutes of Natural Sciences, Aichi 444-8585, Japan.

⁵ Core for Spin Life Sciences, Okazaki Collaborative Platform, National Institutes of Natural Sciences, Aichi 444-8585, Japan.

‡These authors contributed equally.

ABSTRACT

Schottky junctions based on transition-metal dichalcogenides (TMDCs) have emerged as key building blocks for next-generation optoelectronic devices that demand ultrafast response and high sensitivity. However, the ultrafast, nanoscale carrier dynamics at these interfaces—crucial for device performance—have remained experimentally elusive. Here, we introduce optical pump–probe time-resolved atomic force microscopy to directly visualize, in real space, the nanosecond-scale modulation of the Schottky barrier potential at a van der Waals junction formed by point contact between WSe₂ and a PtIr tip. Complementary analyses using transient absorption spectroscopy and light-modulated current-voltage characteristics together with model simulations reveal that time-resolved currents originate from the concerted temporal evolution of photoexcited carriers and the subsequent barrier response—processes that also define the rate-limiting steps of the photocurrent. Our results uncover the essential interfacial dynamics that underpin TMDC-based photodetectors and photovoltaic elements, while establishing a new measurement paradigm that complements and extends existing spectroscopic techniques. This approach provides direct access to nonequilibrium processes hidden at nanoscale interfaces, offering a powerful route to rational design of high-performance optoelectronic devices.

1. Introduction

The advent of two-dimensional materials, particularly transition-metal dichalcogenides (TMDCs), has opened new avenues for the design and performance enhancement of electronic and optoelectronic devices. Owing to their layer-dependent and tunable band structures, together

with their exceptional electrical and optical properties, these materials have become foundational to the continued evolution of semiconductor technologies^{1,2,3}. Among various device architectures, Schottky junctions formed at metal–semiconductor interfaces play a central role not only in electronic devices but also in optoelectronic systems that convert optical energy into electrical signals, as well as in high-efficiency energy-harvesting technologies such as thermoelectric devices^{4,5}. In this context, TMDC-based Schottky junctions are particularly attractive because they combine strong light absorption with excellent carrier transport properties. Moreover, their unique features—such as mechanical flexibility, transferability, and sensitivity to circularly polarized light—offer functionalities that are difficult to achieve with conventional semiconductors. As a result, TMDC-based Schottky junctions have been intensively studied as promising platforms for advancing next-generation energy-harvesting devices^{6,7}.

Despite these advantages, Schottky-based photodetectors employing TMDCs have, to date, exhibited relatively slow response times, typically on the microsecond scale, which has limited their applicability in high-speed optoelectronic technologies. However, recent studies have demonstrated that the use of WSe₂ enables ultrafast photoresponse down to the few-nanosecond regime, highlighting the potential for substantial performance advancements in TMDC-based photodetectors^{8,9,10}. To further enhance device performance, a comprehensive understanding of carrier dynamics at Schottky interfaces and within the TMDC is indispensable, particularly of the ultrafast processes of photoexcited carrier generation, transport, and recombination under optical illumination. Elucidating these dynamic processes is critically important, as they ultimately govern both the response speed and the energy-conversion efficiency of optoelectronic devices.

These photocarrier dynamics are intimately linked to the temporal evolution of the Schottky barrier potential. In addition, van der Waals (vdW) junctions formed between TMDCs and metals constitute intrinsically non-covalent interfaces, characterized by unique interfacial structures such as atomically thin tunneling barriers. As a result, their dynamic response has been reported to differ from that of conventional bulk semiconductor junctions^{11,12,13,14}. Importantly, defect states located near the metal–TMDC interface, which act as interfacial trap states, as well as their spatial distribution, are also expected to play a significant role in determining the response of vdW Schottky junctions^{15,16,17,18}.

To date, a variety of time-resolved approaches—including optical pump–probe spectroscopy and device-based measurements—have been employed to investigate ultrafast processes such as hot-carrier injection¹⁹, thermionic emission¹², and interface-field-driven carrier dynamics²⁰. However, these techniques probe responses that are inherently averaged over the entire device. As a result, they are unable to directly resolve the spatial distribution of carriers in the vicinity of the Schottky interface, nor the spatially inhomogeneous local potential responses arising from surface photovoltage and band-bending modulation. Therefore, to accurately and comprehensively elucidate the local dynamics that govern the performance of TMDC-based devices, there is a strong demand for new experimental approaches that can simultaneously achieve high temporal and spatial resolution.

Here, we employ optical pump–probe time-resolved atomic force microscopy (OPP-TR-AFM), a member of the pump–probe time-resolved scanning probe microscopy (PP-TR-SPM) family^{21,22,23,24,25,26,27}, to elucidate the intrinsic dynamics of TMDC–metal vdW Schottky junctions with both high temporal and spatial resolution. PP-TR-SPM integrates pump–probe methodologies with scanning probe microscopy, thereby enabling the simultaneous achievement

of ultrafast temporal resolution determined by the pulse width and nanometer-scale spatial resolution.

Early implementations of PP-TR-SPM relied on all-electronic voltage-pulse implementations and achieved time-resolved measurements from the picosecond to nanosecond regimes^{28,29,30}. Subsequently, time-resolved scanning tunneling microscopy (STM) combining ultrashort optical pulses enabled access to carrier dynamics spanning from the femtosecond regime to longer timescales, depending on the experimental implementation^{31,32,33,34,35}. More recently, this approach has been extended to terahertz STM (THz-STM)^{36,37,38,39,40,41}, in which sub-cycle pulses are applied as bias voltages, and intensive developments and refinements of this technique have been actively reported.

In this context, OPP-TR-AFM was developed as a powerful approach for probing nanoscale dynamics^{42,43,44,45}. This technique enables the detection of local electrical responses with nanometer-scale spatial resolution, particularly in contact-mode AFM, while minimizing sample damage and avoiding electrode fabrication or lithographic processing^{46,47}.

In this study, we bring a metallic tip into gentle point contact with a bulk WSe₂ under force feedback, thereby forming a vdW Schottky junction *in situ*⁴⁸, and directly visualize its interfacial dynamics at the nanoscale. By establishing a point-contact junction with a bulk WSe₂, a depletion region comparable to that of conventional device architectures is ensured. Furthermore, by adopting a back-illumination geometry, the observed signals can be directly correlated with the intrinsic physics of the Schottky junction.

In addition, we combine OPP-TR-AFM with complementary analyses using picosecond-to-microsecond transient absorption spectroscopy (hereafter ps-TAS) based on the Randomly

Interleaved Pulse Train (RIPT) method⁴⁹, light-modulated current-voltage (I - V) characteristics⁵⁰, and model simulations that qualitatively capture the essential features of the experimental observations. This combined experimental and modeling approach enables a comprehensive evaluation of the interplay between photoexcited carriers and Schottky barrier modulation in TMDC-based junctions. Through this approach, we achieve direct real-space visualization of the concerted response between photoexcited carrier dynamics and the vdW Schottky barrier potential on the nanosecond timescale, together with a consistent physical interpretation supported by the model simulations.

2. Results and Discussion

2.1. OPP-TR-AFM Measurement System

Figure 1a presents an overview of the OPP-TR-AFM system developed in this study. Similar to conventional OPP techniques, a pair of pump and probe pulses separated by a delay time t_d is directed onto the region encompassing the tip apex and the underlying sample surface. Unlike standard OPP measurements, which monitor changes in optical reflectivity or absorption, OPP-TR-AFM equalizes the intensities of the pump and probe pulses and performs time-resolved, local measurements by detecting the t_d -dependent variations in photoinduced currents³¹ or tip-sample interaction forces⁴⁵. In this study, we use contact-mode AFM to form a vdW Schottky junction, in which a PtIr-coated cantilever is brought into gentle point contact with the surface of a bulk WSe₂ single crystal (see Methods for details). The signal of interest is the local current flowing between the tip and the sample, while the tip position is controlled by monitoring the interaction force through standard AFM feedback.

The photoinduced transient current $I_L^*(t_D)$ generated at a delay time $t_d = t_D$ persists until the pump–probe–excited state fully relaxes. Accordingly, the time-resolved signal $I_L(t_D)$ is obtained as the average of $I_L^*(t_d = t_D)$ over one excitation cycle, from $t = 0$ to the laser repetition period τ_R :

$$I_L(t_D) = \frac{1}{\tau_R} \int_0^{\tau_R} I_L^*(t_d = t_D) dt \quad (1)$$

To sensitively detect subtle current variations, we employ lock-in detection. In addition, to minimize the influence of photothermal expansion of the tip and sample, we use the delay-time modulation method³¹. In this approach, rather than modulating the pump or probe pulses themselves for the lock-in reference, the illumination is alternated between two distinct delay times— $t_d = t_D$, the delay of interest, and a sufficiently long delay $t_d = t_{max}$. The lock-in signal is then obtained as the differential current $\Delta I_L(t_D)$ between these two delay conditions:

$$\Delta I_L(t_D) = I_L(t_d = t_D) - I_L(t_d = t_{max}) \quad (2)$$

This approach enables high-sensitivity extraction of the temporal response of the Schottky junction while minimizing thermal artifacts arising from laser illumination.

2.2. WSe₂/PtIr vdW Schottky Junction

To form a vdW Schottky junction, a conductive PtIr-coated cantilever (PF-TUNA, Bruker) was gently brought into contact with a bulk WSe₂ (several micrometers thick), forming a WSe₂/PtIr junction (Fig. 1a). The excitation laser pulses were introduced from the backside of the sample to facilitate future application to practical device evaluation and were focused onto the sample using an aspheric lens (see Methods for details). The WSe₂ surface was prepared by mechanical exfoliation, and its atomically flat morphology was confirmed by STM [Fig. 1b (atomic structure) and Fig. 1c (STM image)]. For the ps-TAS measurements (see Figs. S1 and S2 for details), bulk WSe₂ samples were prepared in the same manner.

2.3. Nanosecond Carrier Dynamics in Bulk WSe₂

To elucidate the carrier dynamics in the WSe₂/PtIr Schottky junction, we first investigate the nanosecond-scale carrier dynamics in bulk WSe₂. Figure 1d shows the band structure of bulk WSe₂⁵¹. The excitations labeled A and B correspond to the interband optical transitions at the K point associated with the A (≈ 1.65 eV) and B (≈ 2.1 eV) excitons, arising from transitions between the conduction-band minimum (denoted C1) and the two spin-orbit-split valence-band states (V1 and V2). The excitation labeled C corresponds to a higher-energy absorption band at 2.4–2.8 eV, which is associated with a high joint density of states in the band-nesting region. These excitations were experimentally confirmed by steady-state absorption spectroscopy (Fig. S2a, top panel). Although several conventions for peak assignment have been reported, we follow Ref. [52] here.

The photon energy of the 488-nm pump pulses used in our experiments (2.54 eV) lies within the C-band transition and excites electrons from the valence band to the conduction band. In monolayer WSe₂, such excitation is known to generate tightly bound excitons with a binding energy of approximately 300 meV^{53,54,55}. In contrast, the exciton binding energy in bulk WSe₂ is much smaller (~ 30 meV), comparable to the thermal energy at room temperature⁵⁶, so that bulk excitons readily dissociate and exhibit picosecond-scale lifetimes⁵⁷.

Previous TAS studies on layered TMDCs have shown that photoexcited carriers undergo rapid energy relaxation and intervalley scattering on femtosecond to picosecond timescales⁵⁸. During this process, the occupation of the band-edge A- and B-exciton states at the K-point does not remain dominant, and the system evolves into a nonequilibrium distribution governed primarily by unbound carriers. Consequently, electrons relax toward the conduction-band minima located between the Γ and K points, resulting in a predominantly free-carrier population⁵⁷. Thus, in our

OPP-TR-AFM measurements, the observed currents primarily probe the concerted dynamics of photo-generated free carriers and the associated modulation of the Schottky barrier.

To clarify the carrier dynamics in bulk WSe₂ on the nanosecond timescale, we examined the delay-time dependence of transient absorption spectra. Previous TAS studies of carrier dynamics in the nanosecond regime remain limited due to constraints in available measurement techniques. To evaluate such processes in our samples, we employed the RIPT method⁴⁹ (see Fig. S1 and Methods for details) and analyzed the transient absorption response as shown in Fig. 1e and Fig. S2.

As seen in Fig. 1e, positive $\Delta T/T$ peaks (A^+ and B^+) appear at the energies corresponding to the static A and B absorption bands. In addition, characteristic negative sidebands (A^- and B^-) are observed on the low-energy tails of these peaks. Similar behavior—on sub-picosecond to nanosecond timescales—has been reported in bulk MoS₂, where these spectral features were interpreted as a photoinduced redshift of the absorption bands associated with excitonic transitions, originating from localized excited species⁵⁹.

The A^+ , B^+ , and associated substructures evolve with delay time. However, these spectral changes (i.e., the shifts or broadening of the A^+ and B^+ tails) do not arise from absorption bleaching of the probe by pump-induced excitons. Instead, they originate from the modification of the excitonic absorption cross-section due to interactions between the excitonic resonances and free carriers generated by the pump and residing near the band edges. Thus, the temporal evolution of these features reflects the lifetime of the photo-generated free-carrier population and can be directly compared with the OPP-TR-AFM observations.

The dynamical evolution of the A^+ peak was similarly observed even at lower pump intensities comparable to those used in the OPP-TR-AFM measurements. As shown in Fig. S2e, the delay-

time dependence of $\Delta T/T$ at the A⁺ wavelength (760 nm) can be well fitted by a tri-exponential function with time constants of 0.9 ns, 3.3 ns, and 75.9 ± 30 ns. According to previous time-resolved microwave conductivity studies, the nanosecond components are attributed to carrier trapping of conduction-band electrons, whereas the tens-of-nanoseconds component corresponds to recombination between trapped electrons and valence-band holes⁶⁰. Later in this work, we compare this longest time constant with the lifetime of holes extracted from OPP-TR-AFM measurements.

2.4. Characteristic Time-Resolved Currents in OPP-TR-AFM

Figure 2 shows representative results from the OPP-TR-AFM measurements. The delay-time modulation method was employed, and the time-resolved current $I_L(t_d)$ is obtained as the differential current defined in Eq. (2). In the actual time-resolved current measurements, the pump and probe pulses have equal intensity and the delay time t_d is swept between $-t_{\max}$ and $+t_{\max}$, giving rise to the symmetric t_d -dependence. As shown in the bias-voltage dependence (Fig. 2a) and excitation-intensity dependence (Fig. 2b), the observed time-resolved currents can be categorized into the following three types:

- (1) Saturation-type response, in which $I_L(t_d)$ increases and saturates with delay time (Fig. 2c; $\Delta I_L(t_d) < 0$);
- (2) Decay-type response, in which $I_L(t_d)$ decreases with delay time (Fig. 2d; $\Delta I_L(t_d) > 0$);
- (3) Coexistence-type response, in which both saturation-type and decay-type components are present (Fig. 2e).

Although spatial variations in the signals were observed, they can be attributed to local factors such as defect distributions (see Fig. 5 for spatial maps). Within the same measurement conditions,

however, the responses can be consistently categorized into the three types described above. As an overall trend, increasing the reverse-bias voltage or decreasing the excitation fluence causes the response to shift in the sequence (saturation-type, Fig. 2c) \rightarrow (coexistence-type, Fig. 2e) \rightarrow (decay-type, Fig. 2d).

In TMDC-based Schottky contacts, the interface forms a vdW junction rather than a chemically bonded interface, implying a weakly coupled structure governed by intermolecular forces¹¹. This configuration suggests the presence of an ultrathin tunneling barrier, and previous studies have reported that the interfacial resistance varies with applied contact pressure⁶¹. AFM measurements offer the advantage of precisely controlling the tip–sample contact force.

Figure 2f shows a representative example of the force dependence of the time-resolved current obtained using this capability. In our experiments, variations in the contact force resulted in noticeable changes in both the signal amplitude and the decay time. However, the absence of a strong nonlinear force dependence and substantial modifications of the decay time indicate that these variations are most likely attributable to changes in the effective contact area, rather than to significant alterations of the interfacial barrier itself. This observation suggests that a stable vdW tunneling barrier is maintained at the interface under our measurement conditions. Interfacial trap states are expected to exist at this vdW tunneling barrier and can play a crucial role in governing the time-resolved carrier dynamics. Previous studies have demonstrated that photoexcited carriers can be captured by such interfacial trap states, resulting in a modification of the Schottky barrier profile⁶². Consequently, surface photovoltage (SPV) effects^{63,64} are likely to make a significant contribution to the time-resolved responses in our measurements.

In the following sections, we develop a model to elucidate the complex, concerted dynamics of photoexcited carriers and Schottky barrier modulation. As a basis for this analysis, we first examine the I - V characteristics using light-modulated current spectroscopy and related techniques.

2.5. Light-Modulated I - V Characteristics: Analysis of the Schottky Barrier

Figure 3a illustrates the band diagrams for different states of the Schottky junction, serving as a basis for interpreting the results. Figure 3a-i shows the band alignment of the tip and sample before contact. Upon mechanical contact, charge redistribution occurs until the Fermi levels align, resulting in the formation of a Schottky barrier ϕ_B (Fig. 3a-ii). When a bias voltage is applied (sample bias voltage V_s), the band structure bends accordingly. Under reverse bias (positive V_s applied to the WSe₂ side), the conduction-band minimum of WSe₂ shifts downward, as illustrated in Fig. 3a-iii. In this regime, the dominant transport mechanism is the thermionic current I_{th} , in which thermally activated electrons flow from the metal tip into WSe₂.

Figure 3a-iv shows the situation under optical excitation. In addition to the thermionic current I_{th} , several photoinduced current components contribute to the total photocurrent. These include the hot-electron current I_{hot} , arising from photoexcited electrons injected into high-energy states, and the hole-diffusion current I_{hole} , in which photoexcited holes diffuse toward and across the interface via interfacial trap states. The tunneling current I_t arises when electrons near the Fermi level of the metal tip tunnel through the barrier, which becomes possible when the barrier height is lowered or its width is reduced.

As shown in Fig. 3b, light-modulated current spectroscopy is performed by periodically switching the illumination on and off while recording the I - V characteristics, enabling simultaneous evaluation of the dark and illuminated current responses^{50,65}. In Fig. 3b, the bias

dependence can be divided into three regimes: (A) the forward-bias region ($V_s < -0.3$ V), (B) the reverse-bias region (-0.3 V $< V_s < +1.5$ V), and (C) the tunneling region ($V_s > +1.5$ V). First, examining the dark I - V curve, we observe a rectifying behavior characteristic of a Schottky junction. The reverse-bias current is dominated by the thermionic current I_{th} , as illustrated in Fig. 3a-iii. Second, the presence of a clear tunneling current I_t in region (C) of Fig. 3b indicates that the depletion width is narrow, suggesting that the WSe₂ surface behaves as a relatively heavily doped n -type semiconductor. Third, in region (C), the onset of the exponential rise shifts depending on the excitation intensity. This behavior indicates the occurrence of a SPV: photoexcited holes are captured at interfacial trap states, modifying (reducing) V_s required to induce tunneling. Such an SPV-induced barrier modulation strongly suggests that a stable vdW tunneling barrier is preserved at the interface under our measurement conditions. Furthermore, from the onset of the forward-bias current, we estimate the Schottky barrier height ϕ_B in Fig. 3a-ii to be approximately ~ 0.6 eV, which, given the highly electron-doped nature of WSe₂, corresponds to the difference between the Fermi levels of PtIr and WSe₂.

2.6. Simultaneous Analysis of the Illuminated DC Current and the Time-Resolved Current:

Visualization of Two Distinct Time-Resolved Current Components

As shown in Fig. 2, the time-resolved current $\Delta I_L(t_d)$ exhibits either negative or positive components depending on the bias voltage and the excitation intensity, and in some cases, both components coexist. To analyze this behavior in detail, we simultaneously measured the illuminated DC (average) current—obtained without delay-time modulation—and the time-resolved current at $t_d = 0$, $\Delta I_L(t_d = 0)$, and examined their bias-voltage dependences. A representative result is shown in Fig. 3c.

In the (A) forward-bias region, a negligibly small but positive photoinduced time-resolved signal $\Delta I_L(t_d = 0)$ is observed. Under forward bias, hole trapping does not occur at the interface, and SPV is absent. Photoexcited electrons generated in WSe₂ flow almost entirely as photocurrent. Thus, the illuminated DC current exhibits a finite value, whereas the differential signal ΔI_L remains nearly zero.

In contrast, in the (B) reverse-bias and (C) tunneling regimes—where pronounced time-resolved changes were observed in Fig. 2a— $\Delta I_L(t_d = 0)$ shows a negative peak around $V_s = +0.3$ V (corresponding to the saturation-type response in Fig. 3c), and with increasing bias voltage, the signal shifts to positive values. Upon entering the tunneling region, both the DC current and $\Delta I_L(t_d = 0)$ increase exponentially.

The transition at $V_s = 0$ V, where $\Delta I_L(t_d = 0)$ begins to shift negative under small positive bias, reflects the onset of SPV generated by hole trapping. Around $V_s = +0.6$ V, the sign of the time-resolved signal $\Delta I_L(t_d = 0)$ reverses. As seen in the $V_s = +0.6$ V trace in Fig. 3d, the time-resolved current consists of a superposition of a saturation-type component and a decay-type component. In other words, the signal evolution corresponds to the sequence defined in Fig. 2—saturation-type \rightarrow coexistence-type \rightarrow decay-type—and cannot be explained merely by a temporal sign change of a single thermionic current. Instead, it reflects the coexistence of two distinct processes that generate negative (saturation-type) and positive (decay-type) contributions.

Figures 3e and 3f show the bias dependence of the amplitude and lifetime extracted from exponential fits to the time-resolved $\Delta I_L(t_d)$. At 100% excitation intensity, the negative component decreases as V_s increases from +0.3 V to +0.6 V, reflecting the reduction of the negative peak observed in Fig. 3d. At the same time, the lifetime exhibits a pronounced change from 40 ns to 20 ns. At $V_s = +0.6$ V, the saturation-type and decay-type responses coexist, whereas for $V_s > +0.6$ V,

the response gradually evolves into a decay-type behavior. At lower excitation intensities of 10% and 50%, only the decay-type response is observed, and the lifetimes show no pronounced dependence on the bias voltage.

Among the four photocurrent components illustrated in Fig. 3a-iv, the hot-electron contribution I_{hot} relaxes within a few picoseconds¹⁹ and therefore does not contribute to the nanosecond-scale signals investigated in this study. In addition, in the bias region of interest (region (B)), the tunneling current I_t is not a dominant component and is thus excluded from the simulations and quantitative analyses discussed below. Accordingly, the time-resolved current $\Delta I_L(t_d)$ observed in this experiment—specifically in region (B) of Fig. 3b and exemplified in Fig. 2—is attributed to the concerted dynamics of two primary contributions: the hole-diffusion current I_{hole} and the thermionic current I_{th} .

2.7. Hole-Diffusion Current I_{hole} and the Origin of the Decay-Type Time-Resolved Current

In a Schottky junction under reverse bias, the dark current is governed by thermionic electrons flowing from the metal into the semiconductor (Fig. 3a-iii). Upon illumination, as described earlier, photoexcited excitons rapidly dissociate into free carriers (electrons and holes). Under reverse bias, photoexcited electrons in the conduction band drift toward the bulk of the semiconductor, while holes in the valence band diffuse toward the interface (Fig. 4a).

In the present WSe₂/PtIr junction, during transport through WSe₂, holes are captured by trap states (in noncontact area) and undergo Shockley–Read–Hall (SRH) recombination^{66,67}, leading to a gradual decay of the hole population (Figs. 4b and 4c). Holes that reach the WSe₂/PtIr interface can tunnel into the PtIr tip through interfacial trap states, giving rise to the hole-diffusion current I_{hole} .

To describe this process quantitatively, we consider a model in which photoexcited holes recombine via trap states through SRH mechanisms during transport. As illustrated in Fig. 4b, when the photoexcited carrier densities satisfy, $\Delta N_p (= \Delta N_e) < N_{\text{dark}}$ in an *n*-type semiconductor, where ΔN_e and ΔN_p denote photoexcited electron and hole densities, respectively, and N_{dark} is the dark electron density, the trap occupancy by electrons is approximately $f \sim 1$. Under these conditions, recombination proceeds efficiently, leading to a short hole lifetime.

In contrast, when $\Delta N_p \gg N_{\text{dark}}$, the trap occupancy of the trap states decreases, approaching a minimum of $f \sim 0.5$ (Fig. 4c)⁶⁸. As the number of unoccupied trap states increases, hole recombination is suppressed and the hole lifetime becomes longer. Therefore, as shown in Fig. 4d, shorter delay times—at which the instantaneous photoexcited carrier densities (ΔN_p and ΔN_e) exceed N_{dark} —lead to longer effective hole lifetimes, resulting in a larger integrated I_{hole} . This behavior naturally produces the decay-type time-resolved current shown on the right side of Fig. 4d. To further support this scenario, Fig. 4e shows the calculated hole lifetime as a function of $\Delta N_p (= \Delta N_e)$ ⁶⁸, demonstrating that the lifetime increases with increasing photoexcited carrier density within the SRH model when trap occupancy is explicitly taken into account.

2.8. Thermionic Current I_{th} and the Origin of the Saturation-Type Time-Resolved Current

We next examine the thermionic current, as illustrated in Fig. 4f. In vdW Schottky junctions, interfacial trap states arise from metal-induced gap states as well as defect-induced gap states at the metal–TMDC interface⁶⁹. Owing to the presence of a vdW tunneling barrier, these interfacial states are weakly coupled to the metal and can therefore retain non-equilibrium charge occupancy. When photoexcited holes are captured by these interfacial trap states, a SPV is generated, leading to a reduction of the band bending. Consequently, as shown in Fig. 4g, the effective Schottky

barrier height decreases, giving rise to an increase in the thermionic current component of the photocurrent.

As the photoexcited carrier density increases further, holes continue to fill the interfacial trap states until electrons are fully depleted from these levels. Under such conditions, the SPV saturates. This mechanism produces the time-resolved current depicted in Fig. 4i. At shorter delay times—when the probe pulse arrives soon after the pump pulse—the instantaneous hole density is higher, and the interfacial trap states remain saturated. As a result, the integrated current becomes smaller than at longer delay times, yielding the characteristic saturation-type time-resolved signal shown on the right side of Fig. 4i.

Based on the above discussion, the decay-type and saturation-type behaviors arise primarily from the two distinct current components, I_{hole} and I_{th} , respectively; thus, their coexistence in the time-resolved current (Figs. 2a and 2e) is entirely feasible. It should be noted that the photogenerated thermionic current I_{th} originates from holes supplied via I_{hole} . Therefore, the time-resolved current associated with I_{th} may also contain a decay-type contribution. This point will be examined later through numerical simulations.

2.9. Model Simulation: Generation of the Time-Resolved Current from Hole-Diffusion Current I_{hole} and Thermionic Current I_{th}

To elucidate the relationship between the measured time-resolved currents and their underlying physical mechanisms, we performed numerical simulations based on the simple model considering the processes described above. We specifically examined the dynamics of the hole-diffusion current I_{hole} and thermionic current I_{th} —both influenced by SRH recombination via trap states, the carrier-density-dependent variation of the recombination lifetime, and the SPV induced by hole

trapping at interface states. Details of the calculation scheme are provided in the Supporting Information.

The hole current consists of two components: (i) an ultrafast contribution from photogenerated holes already located within the depletion region at the moment of excitation (see Eq. S2 in the Supporting Information), and (ii) a delayed contribution from holes generated in the bulk that reach the depletion region by diffusion (see Eq. S3 in the Supporting Information). Under the present experimental conditions—back-side illumination and nanosecond-scale dynamics—the latter contribution dominates the time-resolved signal, as described in section 2.7. and corresponds to the hole-diffusion current I_{hole} . The time-dependent hole-diffusion current was assumed to be proportional to the time-dependent hole concentration N_p in bulk WSe₂ (Eq. S3).

We further assumed that the decay rate of the hole concentration τ_p varies with the hole concentration N_p , because the hole capture rate depends on the number of available recombination centers within the bandgap. Thus, τ_p was treated as a function of the instantaneous hole density, as shown in Fig. 4e (see Eq. S6 in the Supporting Information). In the simulations, τ_p was set to 40 ns at high N_p , a value close to that obtained from the ps-TAS measurements (Fig. S2g), and was assumed to decrease to half of this value (20 ns) at low N_p , corresponding to τ_{p_base} in Eq. S6. In addition, the hole relaxation time in the interfacial trap states, τ_{is} (see Eq. S5 in the Supporting Information), was set to 46 ns at $V_s = +0.3$ V and 31 ns at $V_s = +0.6$ V, values close to those obtained from OPP-TR-AFM measurements (Fig. 3f).

Under these assumptions, the laser-intensity dependence observed in Fig. 2b can be consistently explained, as shown in Fig. 4j. For example, at high excitation intensities, the electron occupancy f of the trap states decreases (Fig. 4c). As a result, the hole lifetime τ_p increases, leading to an enhancement of the hole-diffusion current I_{hole} . This behavior accounts for the responses observed

at 10% and 50% excitation intensities in Fig. 2b. In contrast, at 100% excitation intensity, the contribution of the thermionic current I_{th} becomes dominant over I_{hole} , resulting in the emergence of a saturation-type response.

The magnitude of the thermionic current depends on the effective Schottky barrier height and the applied reverse-bias voltage (see Eq. S1 in the Supporting Information). The effective Schottky barrier height is determined by the degree of hole trapping at interfacial states: a larger number of trapped holes leads to a lower effective barrier height. It is well known that this barrier reduction exhibits a logarithmic dependence on the photoexcited carrier density⁶³. Because the number of holes that can be trapped is limited by the density of interfacial states, this process naturally gives rise to saturation-type behavior in the time-resolved current. Holes trapped at the interfacial states are subsequently released via tunneling of electrons from the tip into these states.

The relaxation time τ_{is} associated with this process depends on the applied reverse-bias voltage, because the number of interfacial states available for hole trapping varies with the bias voltage, which in turn changes the number of states involved in electron tunneling from the tip. In principle, if the energy distribution of interfacial trap states is complex, the relaxation dynamics should be obtained by integrating over both the state distribution and the tunneling probability. Here, for simplicity, we assume a uniform energy distribution of interfacial states, which leads to a relaxation time that scales approximately with the applied bias voltage (see Eq. S5 in the Supporting Information).

Under this assumption, the bias dependence observed in Fig. 2a can be consistently explained (Fig. 4k). For example, at larger reverse-bias voltages, the relaxation time τ_{is} becomes shorter (Eq. S5). As a result, the surface hole density decays more rapidly according to $N_{\text{is}} \propto \exp(-t/\tau_{\text{is}})$, leading to a smaller surface potential change V_{is} (Eq. S4). Consequently, the thermionic current

(saturation-type component) is reduced according to Eq. S1, while the relative contribution of the hole-diffusion current (decay-type component) becomes more pronounced. The opposite trend is expected at lower reverse-bias voltages.

As illustrated in Fig. 4ℓ, the decay-type component in the coexistence-type current originates predominantly from the hole-diffusion current, whereas the saturation-type component is mainly associated with the thermionic current. We note, however, that a minor decay-type contribution is also present in the thermionic channel because the SPV dynamics are governed by hole trapping and detrapping at the interface, which are intrinsically linked to the hole-diffusion process.

Overall, these simulations support the conclusion that the measured time-resolved current arises from the superposition of (i) a decay-type contribution associated with hole transport and SRH recombination, and (ii) a saturation-type contribution, with a minor decay component, associated with thermionic emission modulated by SPV dynamics. The relative amplitudes of these contributions are governed by the applied bias voltage and the excitation intensity.

2.10. Spatial Mapping of the Time-Resolved Current

For the development of next-generation optoelectronic devices, it is essential to obtain a spatiotemporal understanding of carrier dynamics within the material and at its interfaces. In particular, local responses at Schottky junctions and heterointerfaces critically influence device performance. However, conventional optical pump–probe techniques provide only spatially averaged information, making it difficult to directly capture nanoscale inhomogeneities. Motivated by the insights obtained above, we next performed spatial mapping of the time-resolved current using OPP-TR-AFM.

To demonstrate the capability of our measurement technique, we aimed to observe spatial variations in carrier dynamics by identifying regions with inhomogeneous current flow. Time-resolved current mapping was performed over a $4\ \mu\text{m}\times 4\ \mu\text{m}$ area. Figure 5(a) shows the contact-mode AFM topography, and Fig. 5(b) presents the corresponding DC current map acquired simultaneously at V_s of +0.6 V. Even in topographically flat regions with no apparent structural features, the current distribution exhibits substantial spatial variation.

Figures 5(c)–5(f) present spatial maps of the time-resolved current as a function of delay time. By setting the delay time t_d to different values (0, 30, 60, and 120 ns) and scanning the tip, we obtained spatially resolved images of the time-resolved current. The map at $t_d = 0$ clearly shows the coexistence of regions with positive and negative time-resolved current (with red and blue in the colormap indicating positive and negative ΔI_L , respectively).

Figures 5(g) and 5(h) show light-modulated I - V characteristics acquired at representative locations. The illuminated I - V curves differ substantially across positions. At the location marked by the magenta solid circle in Fig. 5a, the onset of forward current occurs at a relatively small negative bias, indicating that the Schottky barrier height ϕ_B is lower. The time-resolved current at that location exhibits a coexistence-type behavior (Fig. 5i). This is consistent with a process in which a lowered ϕ_B enhances the thermionic current I_{th} . From the lifetimes extracted by the fitting analysis (Fig. 5k), it is found that as the thermionic current component I_{th} weakens ($\tau_2 = 19.7$ ns), the contribution of the hole-diffusion current I_{hole} ($\tau_1 = 89.4$ ns) becomes prominent. Consequently, the time-resolved current transitions to a decay-type response, similar to that observed at the blue solid-circle position in Fig. 5(j). This behavior is also consistent with the fact that, for a smaller ϕ_B , the SPV more readily reaches saturation even under the same excitation intensity, thereby

enhancing the saturation-type effect. The hole lifetimes obtained here are in reasonable agreement with the ps-TAS results for the photoexcited carrier lifetime in the bulk.

Possible origins of the variations in barrier height include strain-induced shifts in the band edges, Fermi-level pinning by defect states such as Se vacancies, and vacuum-level shifts arising from interface charges or dipole formation. While disentangling and identifying these contributions will require further study, the ability of our approach to directly image local nonequilibrium dynamics offers an essential basis for such future analyses.

In this work, OPP-TR-AFM enabled spatial mapping of local time-resolved current, allowing us to visualize heterogeneous responses originating from trap states in both interfacial and noncontact regions with nanometer precision. This capability provides new insight essential for the design of next-generation optoelectronic devices and establishes a foundational methodology for probing nonequilibrium interfacial dynamics.

3. Conclusions

Using OPP-TR-AFM, we fabricated a WSe_2/PtIr point-contact vdW Schottky junction and performed the direct visualization of ultrafast interfacial electronic dynamics induced by photoexcitation. The introduction of the delay-time modulation method enabled stable time-resolved current measurements even in the presence of a Schottky barrier. By combining OPP-TR-AFM measurements with complementary experimental analyses based on light-modulated I - V characteristics, which provide direct access to band-structure modulation, ps-TAS, which yields the lifetime of photoexcited holes in the bulk, and numerical simulations that support the physical interpretation of the observed dynamics, we successfully visualized, for the first time, the

nanosecond-scale temporal response of photoexcited carriers together with the associated Schottky-barrier dynamics.

Specifically, we directly and locally resolved, on the nanosecond timescale, the causal sequence linking interfacial trap states at the Schottky junction to SPV, subsequent modulation of the barrier profile, and the resulting temporal evolution of thermionic and hole-diffusion currents. The consistency between the experimental observations and the simulation results provides further support for this picture. This constitutes the first demonstration in which these tightly coupled interfacial processes, which remain obscured in conventional device-averaged measurements, are simultaneously resolved in both space and time.

Moreover, our results reveal that, in vdW Schottky junctions, the presence of an ultrathin tunneling barrier plays a central role in governing the interfacial dynamics. By suppressing direct charge transfer between the TMDC semiconductor and the metal, the vdW tunneling barrier prevents photoexcited holes from being immediately drained into the metal. Instead, the holes are captured by interfacial trap states, where they subsequently recombine with electrons tunneling from the metal. This recombination process gives rise to long-lived non-equilibrium charge accumulation and pronounced modulation of the Schottky barrier, making the interfacial contribution to the time-resolved carrier dynamics particularly pronounced and clearly distinguishable.

The present findings advance the fundamental understanding of ultrafast carrier dynamics at metal–TMDC semiconductor interfaces and provide practical design guidelines for optoelectronic and energy-harvesting devices that demand rapid response. The time-resolved probe microscopy approach introduced here together with supporting model analyses, establishes a new analytical framework for elucidating and optimizing the behavior of next-generation optoelectronic elements,

exemplified by TMDC-based vdW Schottky junctions, and is expected to open new avenues for device engineering.

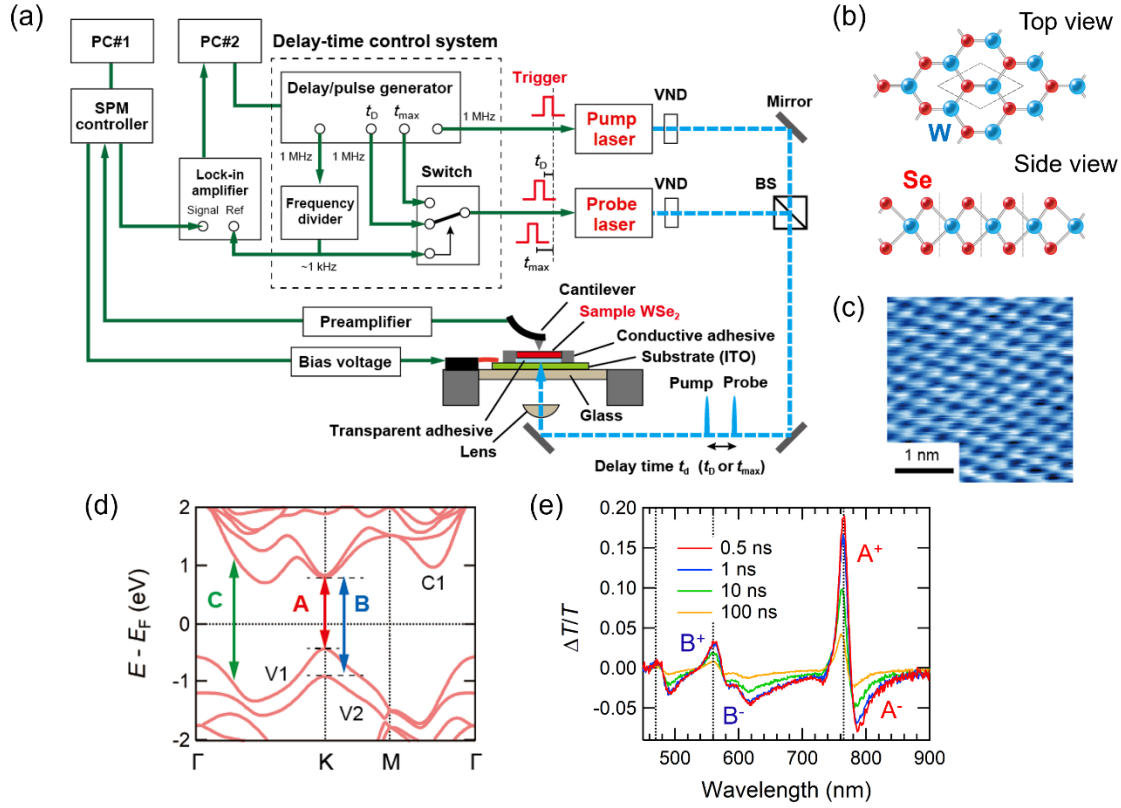


Figure 1. (a) Schematic of the OPP-TR-AFM system. BS: beam splitter, VND: variable neutral density filter. PC#1, PC#2: control computers. t_d : delay-time variable, t_D : selected delay time, t_{max} : long delay time used for the delay-time modulation method. (b) Atomic structure of WSe_2 . (c) STM image of the WSe_2 surface. (d) Band structure of bulk WSe_2 . A and B indicate the direct interband transition energies at the K point, which correspond to the optical transitions giving rise to the A and B excitons, respectively. C denotes the energy range of interband transitions associated with a high joint density of states in the band-nesting region. C1 denotes the conduction-band minimum. V1 and V2 represent the spin-orbit-split valence-band states. (e) Differential transmission spectra $\Delta T/T$ of bulk WSe_2 at $t_d = 0.5, 1, 10,$ and 100 ns under 488-nm excitation obtained by ps-TAS. The resonance features of the fundamental excitations (spectral peak shifts and linewidth changes) are influenced by residual free electrons near the conduction-band edge.

The decay of the photoexcited carrier density over several tens of nanoseconds is clearly observed (see Figs. S1 and S2 for details).

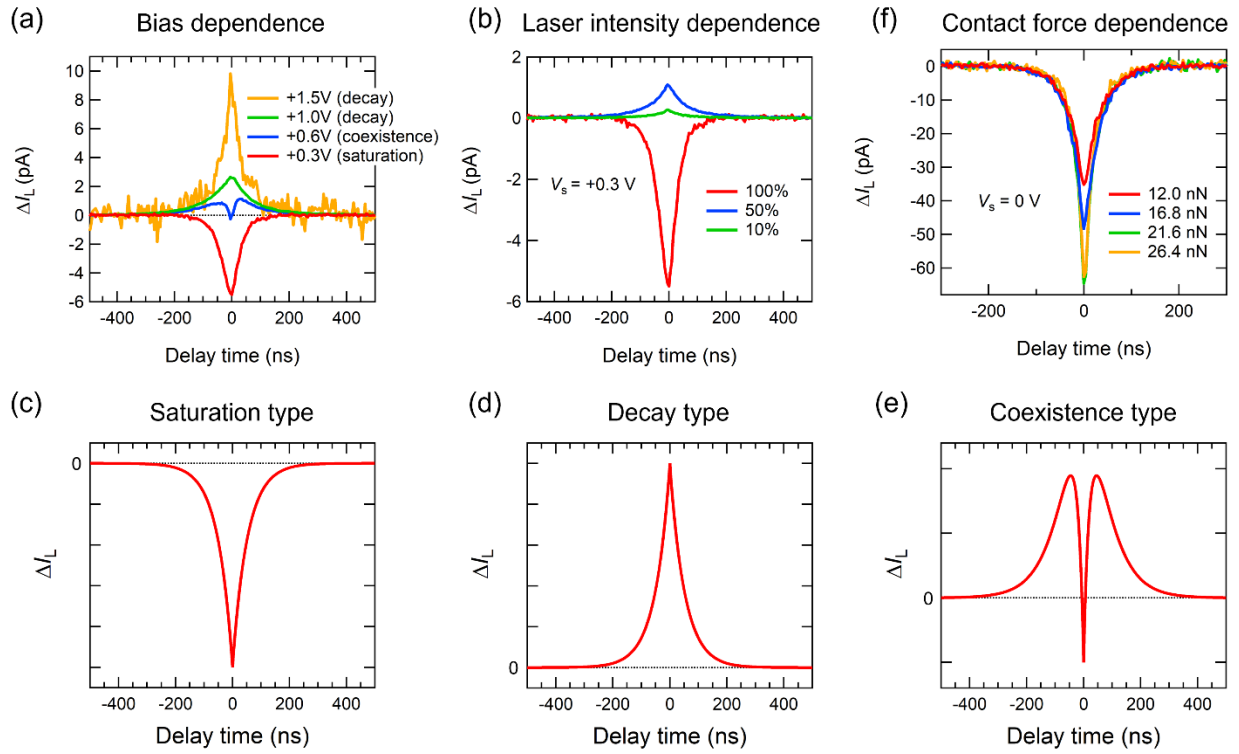


Figure 2. Representative time-resolved currents ΔI_L as a function of delay time t_d obtained using the delay-time modulation method. (a) Dependence on applied sample bias voltage V_s (setpoint force: 12 nN; excitation fluence: $3.4 \mu\text{J cm}^{-2}$). (b) Dependence on excitation fluence (setpoint force: 12 nN; $V_s = +0.3 \text{ V}$; 100% excitation fluence corresponds to $3.4 \mu\text{J cm}^{-2}$). (c-e) The observed time-resolved currents can be classified into three types: (c) saturation-type ($\Delta I_L(t_d) < 0$), (d) decay-type ($\Delta I_L(t_d) > 0$), and (e) coexistence-type, in which both components coexist. (f) Dependence on tip-sample contact force (excitation fluence: $3.0 \mu\text{J cm}^{-2}$; $V_s = 0 \text{ V}$).

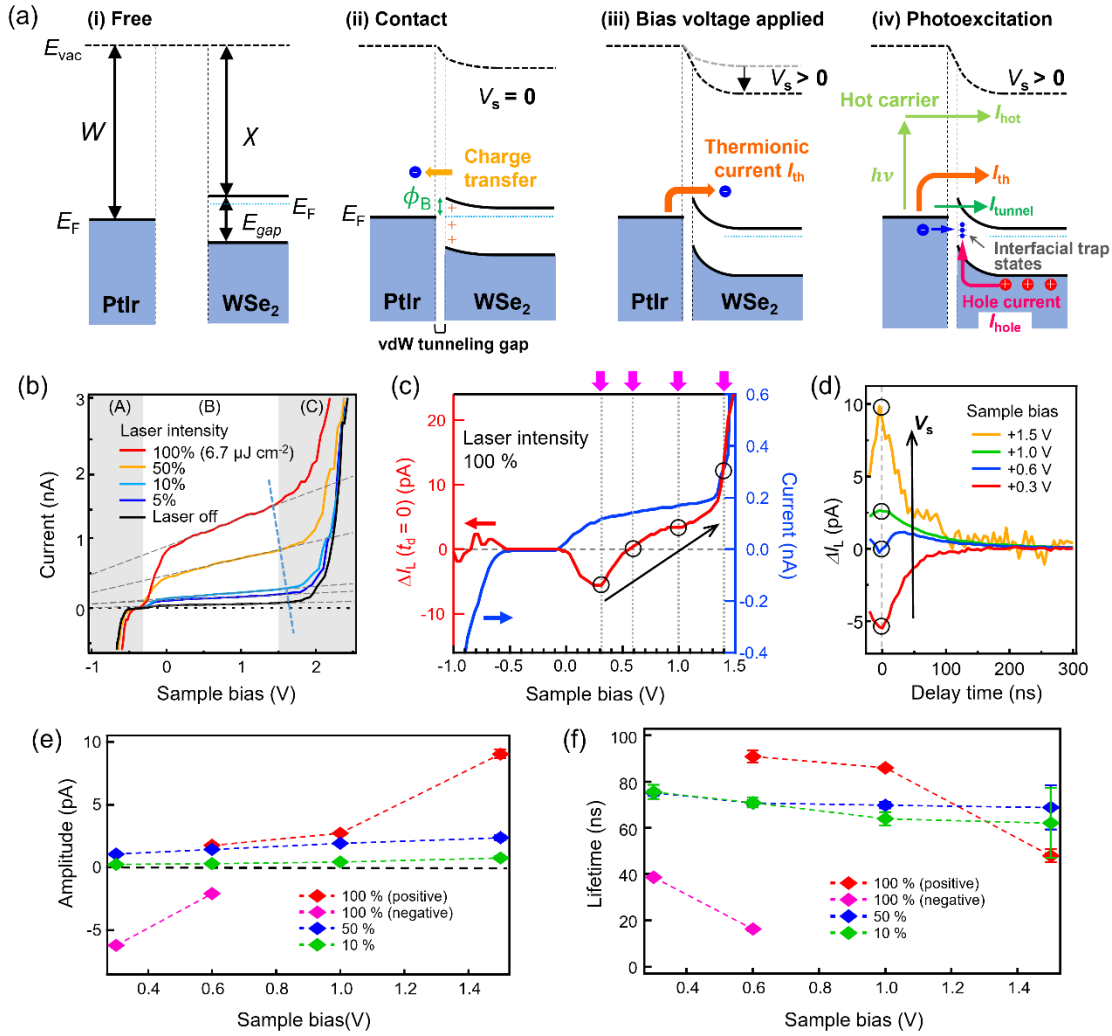


Figure 3. (a) (i) Schematic band diagram of PtIr tip and WSe₂ before contact (W : work function of PtIr, χ : electron affinity of WSe₂). (ii) Band alignment after contact ($V_s = 0$). (iii) Band diagram under an applied sample bias ($V_s > 0$), where a thermionic electron current I_{th} flows over the Schottky barrier. (iv) Band diagram corresponding to (iii) under optical excitation. Possible photocurrent components include: thermionic emission (I_{th} , also present in the dark), hot-electron current I_{hot} arising from photoexcited high-energy electrons, tunneling current I_t that appears at high bias when electrons tunnel through the barrier, and hole-diffusion current I_{hole} , in which photogenerated holes reach interfacial trap states and flow into the metal. Trapping of holes at

interface states produces a SPV, which modifies the barrier height and changes the current. (b) Light-modulated current spectroscopy. I - V curves were acquired while modulating the illumination at 140 Hz. (A) Forward-bias region, (B) reverse-bias region, and (C) tunneling region. The dashed line marks the onset of the tunneling regime. The 100% excitation intensity corresponds to $6.7 \mu\text{J cm}^{-2}$. (c) Bias-voltage dependence of the time-resolved current ΔI_L at $t_d = 0$ and the corresponding DC (total) current for 100% excitation intensity. (d) Time-resolved currents $\Delta I_L(t_d)$ measured at characteristic four V_s indicated by arrows and dotted lines in (c). These data are identical to those shown in Fig. 2(a). At $V_s = +0.6$ V, coexistence of decay-type and saturation-type components is observed. The values of $\Delta I_L(t_d = 0)$ for each bias voltage are highlighted by open circles. The corresponding $\Delta I_L(t_d = 0)$ are also indicated by open circles in (c). (e,f) Bias-voltage dependence of the amplitudes and lifetimes obtained from exponential fitting of the time-resolved current measured at excitation intensities of 10%, 50%, and 100%.

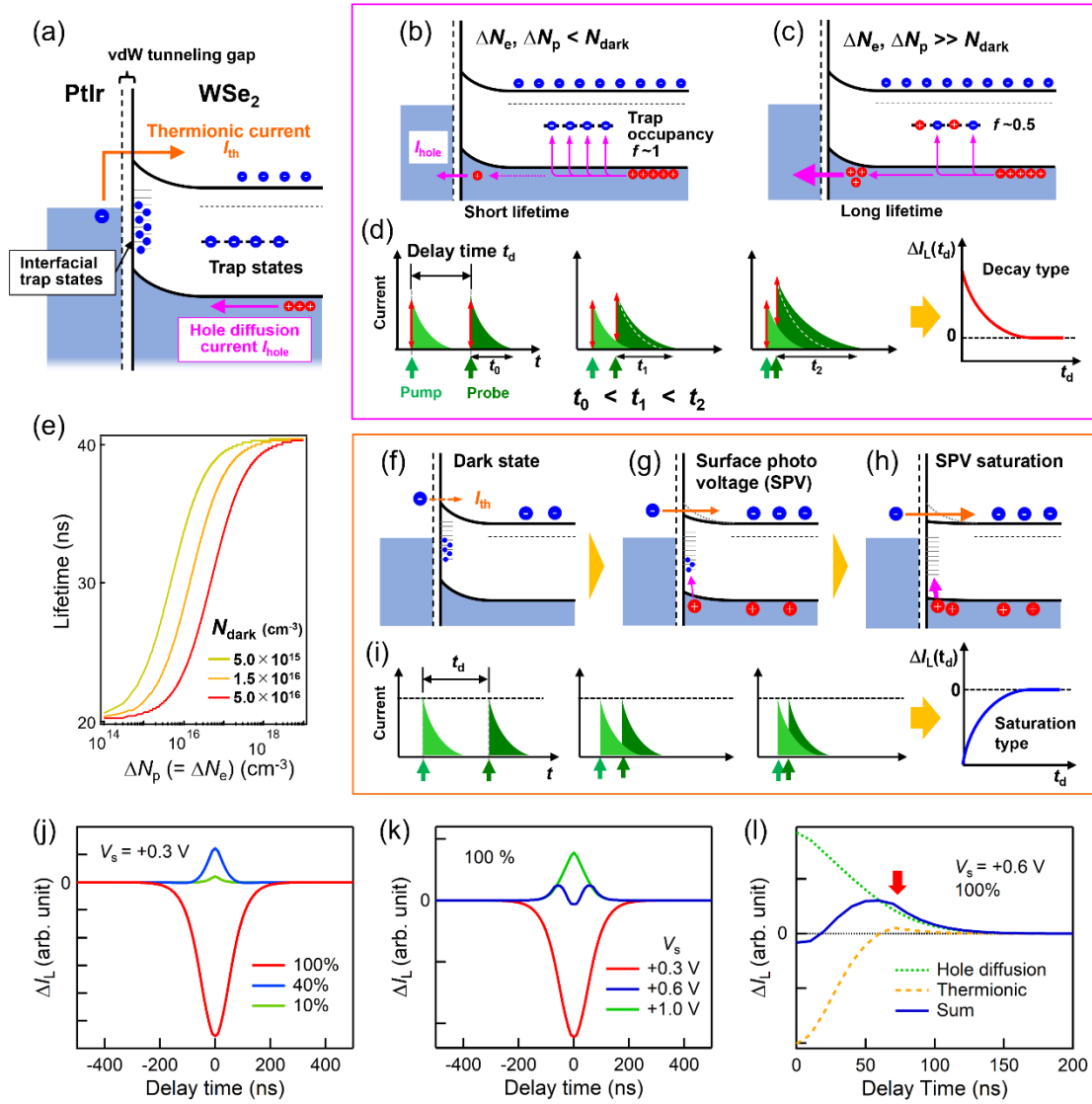


Figure 4. (a) Band diagram of the vdW Schottky junction, illustrating the two current components— hole-diffusion current I_{hole} and thermionic current I_{th} — that primarily contribute to the time-resolved current. $V_s = 0$. (b, c) Variation of I_{hole} arising from SRH recombination via trap states in an n -type semiconductor. Here, ΔN_e and ΔN_p denote the photoexcited electron and hole densities, and N_{dark} the equilibrium electron density. (b) When $\Delta N_e, \Delta N_p < N_{\text{dark}}$ (corresponding to long delay times), efficient SRH recombination shortens the hole lifetime, reducing I_{hole} . (c) When $\Delta N_e, \Delta N_p \gg N_{\text{dark}}$ (short delay times), the trap occupancy decreases ($f \sim 0.5$), suppressing

recombination and increasing the hole lifetime, thereby enhancing I_{hole} . (d) Mechanism for generating the decay-type time-resolved current. (e) Carrier-density dependence of the hole lifetime calculated using an SRH model incorporating trap occupancy. (f-h) Variation of I_{th} induced by the filling and emptying of interfacial trap states at the WSe₂/PtIr junction. (f) Dark condition. (g) Capture of photoexcited holes at interfacial trap states, producing a SPV that lowers the effective Schottky barrier. (h) At sufficiently high hole densities, interfacial trap states become saturated, leading to saturation of the photocurrent. (i) Origin of the saturation-type time-resolved current arising from SPV saturation. (j) Calculated excitation-density dependence of the time-resolved current. (k) Calculated bias dependence. (l) Decomposition of the time-resolved current into contributions from I_{hole} and I_{th} for 100% excitation at V_s of +0.6 V in (k). The red arrow indicates a region where the combined signal exceeds the contribution from I_{hole} , demonstrating that the thermionic component contains a subtle decay-like contribution.

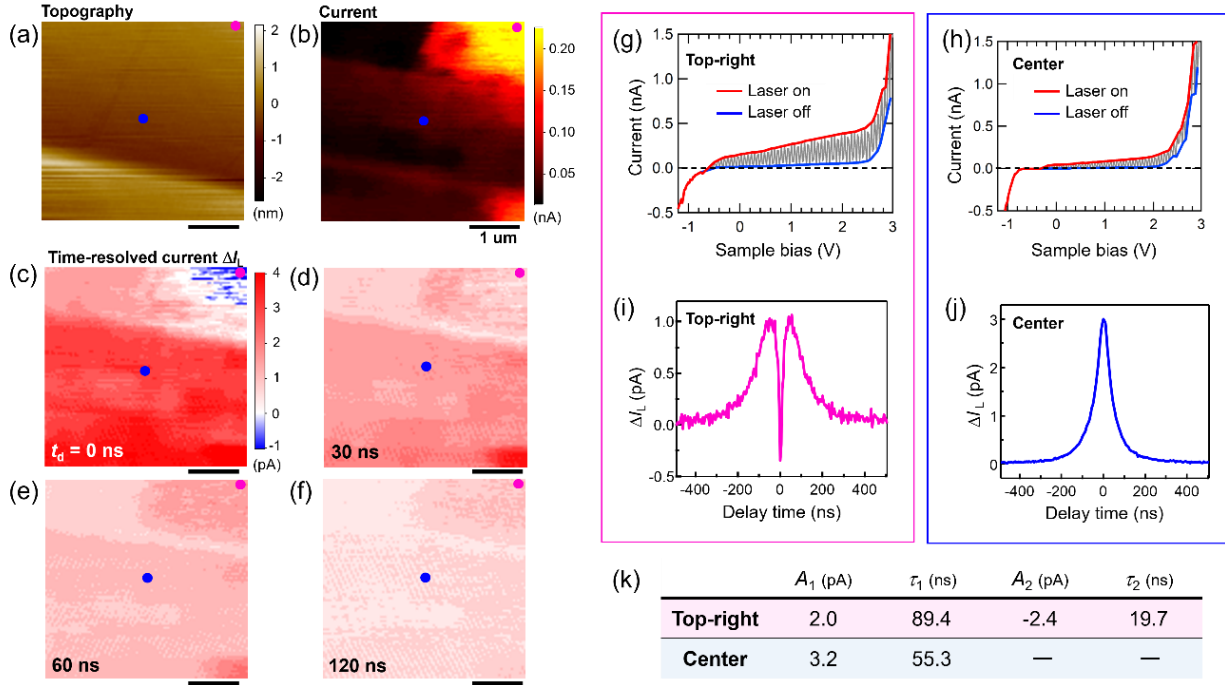


Figure 5. (a) Contact-mode AFM image ($4 \mu\text{m} \times 4 \mu\text{m}$, setpoint: 16.8 nN) (b) Simultaneously acquired DC current map at $V_s = +0.6$ V. The solid-circle markers indicate the positions where light-modulated I - V characteristics and time-resolved currents were measured. (c-f) Time-resolved current maps at delay times $t_d = 0, 30, 60,$ and 120 ns, respectively ($V_s = +0.6$ V). (g, h) Light-modulated I - V curves at the positions marked in blue and magenta, respectively (excitation fluence: $6.7 \mu\text{J cm}^{-2}$). (i, j) Delay-time dependence of the time-resolved current at the magenta and blue marker positions, respectively ($V_s = +0.6$ V, setpoint: 14.4 nN). (k) Amplitudes and lifetimes of the coexistence-type components (A_1, τ_1, A_2, τ_2) and decay-type component (A_1, τ_1), obtained by exponential fitting the data in (i) and (j).

Methods

Optical System for OPP-TR-AFM

The laser pulses are precisely synchronized using an electronic trigger, enabling a simple configuration that does not require a complex optical setup (OPP-NS, Unisoku)^{70,71}. In this study, we focus on nanosecond dynamics that reflect the characteristic timescales of the Schottky barrier and interfacial trap state processes. Accordingly, we employed two nanosecond pulsed lasers (NPL49B, Thorlabs) as the pump and probe sources. Both lasers operated at a wavelength of 488 nm, with a pulse width of approximately 6 ns and a repetition rate of 1 MHz. The timing jitter between the two lasers with respect to the electronic trigger was approximately 20 ps, and the overall temporal resolution of the system was estimated to be ~8.5 ns. To ensure broad applicability for various materials and device-oriented studies, the system is combined with an ambient AFM setup (Dimension XR Icon, Bruker), and all measurements were performed at room temperature under ambient conditions.

Sample Preparation

To enable backside optical excitation, a bulk WSe₂ single crystal (HQ Graphene) was mounted onto a conductive ITO-coated glass substrate using a transparent epoxy adhesive (FH5313PK, Thorlabs). For stable current acquisition in contact-mode AFM measurements, a conductive silver epoxy (EPO-TEK H20E) was used between the WSe₂ crystal and the ITO substrate to ensure a reliable electrical connection. During measurements, the ITO substrate (and the attached sample) was placed on the glass plate of the SPM sample stage and secured using a magnetic contact pin (Fig. 1a). The contact pin also served as an electrode, allowing bias voltages to be applied to the sample. In this configuration, two metal–WSe₂ junctions exist: one at the cantilever–WSe₂ point

contact and the other at the ITO substrate– WSe₂ interface. Previous studies have shown that the dominant contribution to the measured current originates from the point contact between the AFM tip and the WSe₂ sample¹⁷.

Picosecond-to-Microsecond Transient Absorption Spectroscopy (ps-TAS)

In conventional transient absorption spectroscopy, the time window from approximately 1 ns to several tens of nanoseconds has been a “blind gap,” largely because it is difficult to continuously vary the pump–probe delay within this regime using standard delay-line optics. To overcome this limitation, we utilized a commercially available picosecond transient absorption system, picoTAS (Unisoku), based on the RIPT method (see Supporting Information). This technique, which we previously developed, enables asynchronous and randomized sampling of pump–probe delays using a picosecond supercontinuum laser as the probe light, thereby providing access to this otherwise inaccessible temporal region⁴⁹.

For the pump pulses, we used a 1 kHz, 25 ps mode-locked picosecond laser equipped with a tunable wavelength unit (PL2210A and PG403, EKSPLA). The pump wavelength was set to 488 nm to allow direct comparison with the OPP-TR-AFM measurements. As the probe source, we used a 20 MHz, 50-100 ps supercontinuum laser (SMHP-20.2-A, Leukos), spectrally selected by a diffraction-grating monochromator to cover the wavelength range from 450 to 900 nm. Temporal resolution of the system was better than 100 ps and was primarily determined by the pulse width of the probe light. All ps-TAS measurements were performed at room temperature under ambient conditions.

Author Contributions

OPP-TR-AFM experiments were performed by M.Y., K.I., and T.M., while the ps-TAS measurements were carried out by T.N. S.Y. and O.T. provided technical advice on sample preparation and experimental methodologies. The mechanism of photoinduced dynamics at the Schottky junction was primarily conceived by H.M., Y.M., M.Y., and H.S., and was further established through combined investigations of time-resolved signal simulations by Y.M. and analyses of I - V characteristics by H.M. The project was organized and supervised by K.I. and H.S., who coordinated the overall research effort.

Data Availability

The data that support the findings of the study are available from the corresponding authors upon reasonable request.

Notes

The authors declare no competing financial interest.

ACKNOWLEDGMENTS

The authors express their gratitude to Tadashi Ueda (IMS) and Shunji Yamamoto (Unisoku) for their technical support.

This work was supported by JSPS KAKENHI (Grant Nos. 23H00264, 24H00416, and 25H00835) and by JST PRESTO (Grant No. JPMJPR22AA).

REFERENCES

¹ Xia, F.; Wang, H.; Xiao, D.; Dubey, M.; Ramasubramaniam, A. Two-Dimensional Material Nanophotonics. *Nature Photon.* **2014**, *8*, 899–907. DOI: 10.1038/nphoton.2014.271

² Koppens, F. H. L.; Mueller, T.; Avouris, P.; Ferrari, A. C.; Vitiello, M. S.; Polini, M. Photodetectors Based on Graphene, Other Two-Dimensional Materials and Hybrid Systems. *Nat. Nanotechnol.* **2014**, *9*, 780–793. DOI: 10.1038/nnano.2014.215

³ Fiori, G.; Bonaccorso, F.; Iannaccone, G.; Palacios, T.; Neumaier, D.; Seabaugh, A.; Banerjee, S. K.; Colombo, L. Electronics Based on Two-Dimensional Materials. *Nat. Nanotechnol.* **2014**, *9*, 768–779. DOI: 10.1038/nnano.2014.207

⁴ Xu, Y.; Cheng, C.; Du, S.; Yang, J.; Yu, B.; Luo, J.; Yin, W.; Li, E.; Dong, S.; Ye, P.; Duan, X. Contacts between Two- and Three-Dimensional Materials: Ohmic, Schottky, and *p-n* Heterojunctions. *ACS Nano* **2016**, *10*, 4895–4919. DOI: 10.1021/acsnano.6b01842

⁵ Tung, R. T. The Physics and Chemistry of the Schottky Barrier Height. *Appl. Phys. Rev.* **2014**, *1*, 011304. DOI: 10.1063/1.4858400

⁶ Lopez-Sanchez, O.; Lembke, D.; Kayci, M.; Radenovic, A.; Kis, A. Ultrasensitive Photodetectors Based on Monolayer MoS₂. *Nat. Nanotechnol.* **2013**, *8*, 497–501. DOI: 10.1038/nnano.2013.100

⁷ Liu, X.; Choi, M. S.; Hwang, E.; Yoo, W. J.; Sun, J. Fermi Level Pinning Dependent 2D Semiconductor Devices: Challenges and Prospects. *Adv. Mater.* **2022**, *34*, 2108425. DOI: 10.1002/adma.202108425

⁸ Zhang, Y.; Shen, W.; Wu, S.; Tang, W.; Shu, Y.; Ma, K.; Zhang, B.; Zhou, P.; Wang, S. High-Speed Transition-Metal Dichalcogenides Based Schottky Photodiodes for Visible and Infrared Light Communication. *ACS Nano* **2022**, *16*, 19187–19198. DOI: 10.1021/acsnano.2c08394

⁹ Strauß, F.; Kohlschreiber, P.; Keck, J.; Michel, P.; Hiller, J.; Meixner, A. J.; Scheele, M. A Simple 230 MHz Photodetector Based on Exfoliated WSe₂ Multilayers. *RSC Appl. Interfaces* **2024**, *1*, 728–733. DOI: 10.1039/D4LF00019F

¹⁰ Zhang, M.; Liu, X.; Duan, X.; Zhang, S.; Liu, C.; Wan, D.; Li, G.; Xia, Z.; Fan, Z.; Liao, L. Schottky-Contacted WSe₂ Hot-Electron Photodetectors with Fast Response and High Sensitivity. *ACS Photonics* **2021**, *8*, 132–137. DOI: 10.1021/acsp Photonics.1c01256

¹¹ Kong, L.; Zhang, X.; Tao, Q.; Zhang, M.; Dang, W.; Li, Z.; Feng, L.; Liao, L.; Duan, X.; Liu, Y. Doping-Free Complementary WSe₂ Circuit via van der Waals Metal Integration. *Nat. Commun.* **2020**, *11*, 1866. DOI: 10.1038/s41467-020-15776-X

¹² Keller, K. R.; Rojas-Aedo, R.; Zhang, H.; Schweizer, P.; Allerbeck, J.; Brida, D.; Jariwala, D.; Maccaferri, N. Ultrafast Thermionic Electron Injection Effects on Exciton Formation Dynamics at a van der Waals Semiconductor/Metal Interface. *ACS Photonics* **2022**, *9*, 2683–2690. DOI: 10.1021/acsp Photonics.2c00394

¹³ Wang, Y.; Kim, J. C.; Wu, R. J.; Martinez, J.; Song, X.; Yang, J.; Zhao, F.; Mkhoyan, A. V.; Jeong, H. Y.; Chhowalla, M. Van der Waals Contacts between Three-Dimensional Metals and Two-Dimensional Semiconductors. *Nature* **2019**, *568*, 70–74. DOI: 10.1038/s41586-019-1052-3

¹⁴ Allain, A.; Kang, J.; Banerjee, K.; Kis, A. Electrical Contacts to Two-Dimensional Semiconductors. *Nat. Mater.* **2015**, *14*, 1195–1205. DOI: 10.1038/nmat4452

¹⁵ Bampoulis, P.; van Bremen, R.; Yao, Q.; Poelsema, B.; Zandvliet, H. J. W.; Sotthewes, K. Defect-Dominated Charge Transport and Fermi Level Pinning in MoS₂/Metal Contacts. *ACS Appl. Mater. Interfaces* **2017**, *9*, 19278–19286. DOI: 10.1021/acsami.7b02739

¹⁶ Sotthewes, K.; van Bremen, R.; Dollekamp, E.; Boulogne, T.; Nowakowski, K.; Kas, D.; Zandvliet, H. J. W.; Bampoulis, P. Universal Fermi-Level Pinning in Transition-Metal Dichalcogenides. *J. Phys. Chem. C* **2019**, *123*, 5411–5418. DOI: 10.1021/acs.jpcc.8b10971

¹⁷ Giannazzo, F.; Fisichella, G.; Piazza, A.; Agnello, S.; Roccaforte, F. Nanoscale Inhomogeneity of the Schottky Barrier and Resistivity in MoS₂ Multilayers. *Phys. Rev. B* **2015**, *92*, 081307(R). DOI: 10.1103/PhysRevB.92.081307

¹⁸ Hong, C.; Kim, H.; Tao, Y.; Lim, J.; Lee, J.; Kim, J. Ultrafast Hot Carrier Extraction and Diffusion at the MoS₂/Au van der Waals Electrode Interface. *Sci. Adv.* **2025**, *11*, eadr1534. DOI: 10.1126/sciadv.adr1534

¹⁹ Chen, D.; Anantharaman, S. B.; Wu, J.; Qiu, D. Y.; Jariwala, D.; Guo, P. Optical Spectroscopic Detection of Schottky Barrier Height at a Two-Dimensional Transition-Metal Dichalcogenide/Metal Interface. *Nanoscale* **2024**, *16*, 5169–5176. DOI: 10.1039/D3NR05799B

²⁰ Tao, Y.; Hong, C.; Kim, J. Ultrafast Reversible Photoconductivity in 2D MoTe₂/Pt van der Waals Heterostructure. *Sci. Adv.* **2025**, *11*, eady1321. DOI: 10.1126/sciadv.ady1321

²¹ Terada, Y.; Yoshida, S.; Takeuchi, O.; Shigekawa, H. Laser-Combined Scanning Tunnelling Microscopy for Probing Ultrafast Transient Dynamics. *J. Phys.: Condens. Matter* **2010**, *22*, 264008. DOI: 10.1088/0953-8984/22/26/264008

²² van Houselt, A.; Zandvliet, H. J. W. Colloquium: Time-Resolved Scanning Tunneling Microscopy. *Rev. Mod. Phys.* **2010**, *82*, 1593–1630. DOI: 10.1103/RevModPhys.82.1593

²³ Yoshida, S.; Terada, Y.; Yokota, M.; Takeuchi, O.; Oigawa, H.; Shigekawa, H. Optical Pump-Probe Scanning Tunneling Microscopy for Probing Ultrafast Dynamics on the Nanoscale. *Eur. Phys. J. Spec. Top.* **2013**, *222*, 1161–1175. DOI: 10.1140/epjst/e2013-01912-2

²⁴ Mascaro, A.; Miyahara, Y.; Enright, T.; Dagdeviren, O. E.; Grütter, P. Review of Time-Resolved Non-Contact Electrostatic Force Microscopy Techniques with Applications to Ionic Transport Measurements. *Beilstein J. Nanotechnol.* **2019**, *10*, 617–633. DOI: 10.3762/bjnano.10.62

²⁵ Araki, K.; Ie, Y.; Aso, Y.; Ohoyama, H.; Matsumoto, T. Time-Resolved Electrostatic Force Microscopy Using Tip-Synchronized Charge Generation with Pulsed Laser Excitation. *Commun. Phys.* **2019**, *2*, 10. DOI: 10.1038/s42005-019-0108-x

²⁶ Liang, K.; Bi, L.; Zhu, Q.; Zhou, H.; Li, S. Ultrafast Dynamics Revealed with Time-Resolved Scanning Tunneling Microscopy: A Review. *ACS Appl. Opt. Mater.* **2023**, *1*, 924–938. DOI: 10.1021/acsaom.2c00169

²⁷ Wang, Y.; Nishida, J.; Nakamoto, K.; Yang, X.; Sakuma, Y.; Zhang, W.; Endo, T.; Miyata, Y.; Kumagai, T. Ultrafast Nano-Imaging of Spatially Modulated Many-Body Dynamics in CVD-Grown Monolayer WS₂. *ACS Photonics* **2025**, *12*, 207–218. DOI: 10.1021/acsp Photonics.4c01545

²⁸ Nunes, G., Jr.; Freeman, M. R. Picosecond Resolution in Scanning Tunneling Microscopy. *Science* **1993**, *262*, 1029–1032. DOI: 10.1126/science.262.5136.1029

²⁹ Loth, S.; Etzkorn, M.; Lutz, C. P.; Eigler, D. M.; Heinrich, A. J. Measurement of Fast Electron Spin Relaxation Times with Atomic Resolution. *Science* **2010**, *329*, 1628–1630. DOI: 10.1126/science.1191688

³⁰ Friedlein, J.; Harm, J.; Lindner, P.; Bargsten, L.; Bazarnik, M.; Krause, S.; Wiesendanger, R. A Radio-Frequency Spin-Polarized Scanning Tunneling Microscope. *Rev. Sci. Instrum.* **2019**, *90*, 123705. DOI: 10.1063/1.5104317

³¹ Terada, Y.; Yoshida, S.; Takeuchi, O.; Shigekawa, H. Real-Space Imaging of Transient Carrier Dynamics by Nanoscale Pump–Probe Microscopy. *Nature Photon.* **2010**, *4*, 869–874. DOI: 10.1038/nphoton.2010.235

³² Yoshida, S.; Yokota, M.; Takeuchi, O.; Oigawa, H.; Mera, Y.; Shigekawa, H. Single-Atomic-Level Probe of Transient Carrier Dynamics by Laser-Combined Scanning Tunneling Microscopy. *Appl. Phys. Express* **2013**, *6*, 032401. DOI: 10.7567/APEX.6.032401

³³ Li, S.; Chen, S.; Li, J.; Wu, R.; Ho, W. Joint Space-Time Coherent Vibration Driven Conformational Transitions in a Single Molecule. *Phys. Rev. Lett.* **2017**, *119*, 176002. DOI: 10.1103/PhysRevLett.119.176002

³⁴ Kloth, P.; Wenderoth, M. From Time-Resolved Atomic-Scale Imaging of Individual Donors to Their Cooperative Dynamics. *Sci. Adv.* **2017**, *3*, e1601552. DOI: 10.1126/sciadv.1601552

³⁵ Guo, C.; Meng, X.; Fu, H.; Wang, Q.; Wang, H.; Tian, Y.; Peng, J.; Ma, R.; Weng, Y.; Meng, S.; Wang, E.; Jiang, Y. Probing Nonequilibrium Dynamics of Photoexcited Polarons on a Metal-Oxide Surface with Atomic Precision. *Phys. Rev. Lett.* **2020**, *124*, 206801. DOI: 10.1103/PhysRevLett.124.206801

³⁶ Cocker, T. L.; Jelic, V.; Gupta, M.; Molesky, S. J.; Burgess, J. A. J.; De Los Reyes, G.; Titova, L. V.; Tsui, Y. Y.; Freeman, M. R.; Hegmann, F. A. An Ultrafast Terahertz Scanning Tunneling Microscope. *Nature Photon.* **2013**, *7*, 620–625. DOI: 10.1038/nphoton.2013.151

³⁷ Cocker, T. L.; Peller, D.; Yu, P.; Repp, J.; Huber, R. Tracking the Ultrafast Motion of a Single Molecule by Femtosecond Orbital Imaging. *Nature* **2016**, *539*, 263–267. DOI: 10.1038/nature19816

³⁸ Yoshida, S.; Arashida, Y.; Hirori, H.; Tachizaki, T.; Taninaka, A.; Ueno, H.; Takeuchi, O.; Shigekawa, H. Terahertz Scanning Tunneling Microscopy for Visualizing Ultrafast Electron Motion in Nanoscale Potential Variations. *ACS Photonics* **2021**, *8*, 315–323. DOI: 10.1021/acsp Photonics.0c01572

³⁹ Arashida, Y.; Mogi, H.; Ishikawa, M.; Igarashi, I.; Hatanaka, A.; Umeda, N.; Peng, J.; Yoshida, S.; Takeuchi, O.; Shigekawa, H. Subcycle Mid-Infrared Electric-Field-Driven Scanning Tunneling Microscopy with a Time Resolution Higher Than 30 fs. *ACS Photonics* **2022**, *9*, 3156–3164. DOI: 10.1021/acsp Photonics.2c00995

⁴⁰ Garg, M.; Kern, K. Attosecond Coherent Manipulation of Electrons in Tunneling Microscopy. *Science* **2019**, *367*, 411–415. DOI: 10.1126/science.aaz1098

⁴¹ Kimura, K.; Tamaki, R.; Lee, M.; Ouyang, X.; Kusaba, S.; Jaculbia, R. B.; Kawada, Y.; Jung, J.; Muranaka, A.; Imada, H.; Katayama, I.; Takeda, J.; Kim, Y. Ultrafast On-Demand Exciton Formation in a Single-Molecule Junction by Tailored Terahertz Pulses. *Science* **2025**, *387*, 1077–1082. DOI: 10.1126/science.ads2776

⁴² Kajimoto, K.; Araki, K.; Usami, Y.; Ohoyama, H.; Matsumoto, T. Visualization of Charge Migration in Conductive Polymers via Time-Resolved Electrostatic Force Microscopy. *J. Phys. Chem. A* **2020**, *124*, 5063–5070. DOI: 10.1021/acs.jpca.9b12017

⁴³ Schumacher, Z.; Spielhofer, A.; Miyahara, Y.; Grütter, P. The Limit of Time Resolution in Frequency Modulation Atomic Force Microscopy by a Pump–Probe Approach. *Appl. Phys. Lett.* **2017**, *110*, 053111. DOI: 10.1063/1.4975629

⁴⁴ Jahng, J.; Brocious, J.; Fishman, D. A.; Yampolsky, S.; Nowak, D.; Huang, F.; Apkarian, V. A.; Wickramasinghe, H. K.; Potma, E. O. Ultrafast Pump-Probe Force Microscopy with Nanoscale Resolution. *Appl. Phys. Lett.* **2015**, *106*, 083113. DOI: 10.1063/1.4913853

⁴⁵ Mogi, H.; Wakabayashi, R.; Yoshida, S.; Arashida, Y.; Taninaka, A.; Iwaya, K.; Miura, T.; Takeuchi, O.; Shigekawa, H. Time-Resolved Force Microscopy Using the Delay-Time Modulation Method. *Appl. Phys. Express* **2024**, *17*, 015003. DOI: 10.35848/1882-0786/ad0c04

⁴⁶ Mogi, H.; Wang, Z.-H.; Bamba, T.; Takaguchi, Y.; Endo, T.; Yoshida, S.; Taninaka, A.; Oigawa, H.; Miyata, Y.; Takeuchi, O.; Shigekawa, H. Development of Laser-Combined Scanning Multiprobe Spectroscopy and Application to Analysis of WSe₂/MoSe₂ In-Plane Heterostructure. *Appl. Phys. Express* **2019**, *12*, 045002. DOI: 10.7567/1882-0786/ab09b9

⁴⁷ Mogi, H.; Wang, Z.-h.; Kuroda, I.; Takaguchi, Y.; Miyata, Y.; Taninaka, A.; Arashida, Y.; Yoshida, S.; Takeuchi, O.; Shigekawa, H. Laser-Combined Multiprobe Microscopy and Its Application to the Materials with Atomic Layer Thickness. *Jpn. J. Appl. Phys.* **2022**, *61*, SL1011. DOI: 10.35848/1347-4065/ac6a3c

⁴⁸ Gurarslan, A.; Jiao, S.; Li, T.-D.; Li, G.; Yu, Y.; Gao, Y.; Riedo, E.; Xu, Z.; Cao, L. Van der Waals Force Isolation of Monolayer MoS₂. *Adv. Mater.* **2016**, *28*, 10055–10060. DOI: 10.1002/adma.201601581

⁴⁹ Nakagawa, T.; Okamoto, K.; Hanada, H.; Katoh, R. Probing with Randomly Interleaved Pulse Train Bridges the Gap between Ultrafast Pump-Probe and Nanosecond Flash Photolysis. *Opt. Lett.* **2016**, *41*, 1498–1501. DOI: 10.1364/OL.41.001498

⁵⁰ Takeuchi, O.; Yoshida, S.; Shigekawa, H. Light-Modulated Scanning Tunneling Spectroscopy for Nanoscale Imaging of Surface Photovoltage. *Appl. Phys. Lett.* **2004**, *84*, 3645–3647. DOI: 10.1063/1.1737063

⁵¹ Chen, X.; Wang, Z.; Wang, L.; Wang, H.-Y.; Yue, Y.-Y.; Wang, H.; Wang, X.-P.; Wee, A. T. S.; Qiu, C.-W.; Sun, H.-B. Investigating the Dynamics of Excitons in Monolayer WSe₂ before and after Organic Super Acide Treatment. *Nanoscale* **2018**, *10*, 9346–9352. DOI: 10.1039/C8NR00774H

⁵² Mishra, H.; Bose, A.; Dhar, A.; Bhattacharya, S. Exciton-Phonon Coupling and Band-Gap Renormalization in Monolayer WSe₂. *Phys. Rev. B* **2018**, *98*, 045143. DOI: 10.1103/PhysRevB.98.045143

⁵³ Zhao, W.; Ghorannevis, Z.; Chu, L.; Toh, M.; Kloc, C.; Tan, P.-H.; Eda, G. Evolution of Electronic Structure in Atomically Thin Sheets of WS₂ and WSe₂. *ACS Nano* **2013**, *7*, 791–797. DOI: 10.1021/nn305275h

⁵⁴ Zhao, W.; Ghorannevis, Z.; Amara, K. K.; Pang, J. R.; Toh, M.; Zhang, X.; Kloc, C.; Tan, P.-H.; Eda, G. Lattice Dynamics in Mono- and Few-Layer Sheets of WS₂ and WSe₂. *Nanoscale* **2013**, *5*, 9677–9683. DOI: 10.1039/C3NR03052K

⁵⁵ Arora, A.; Koperski, M.; Nogajewski, K.; Marcus, J.; Faugeras, C.; Potemski, M. Excitonic Resonances in Thin Films of WSe₂: From Monolayer to Bulk Material. *Nanoscale* **2015**, *7*, 10421–10429. DOI: 10.1039/C5NR01536G

⁵⁶ Schuster, R.; Wan, Y.; Knupfer, M.; Büchner, B. Nongeneric Dispersion of Excitons in the Bulk of WSe₂. *Phys. Rev. B* **2016**, *94*, 085201. DOI: 10.1103/PhysRevB.94.085201

⁵⁷ Völzer, T.; Lütgens, M.; Fennel, F.; Lochbrunner, S. Recombination Dynamics of Optically Excited Charge Carriers in Bulk MoS₂. *J. Phys. B: At. Mol. Opt. Phys.* **2017**, *50*, 194003. DOI: 10.1088/1361-6455/aa89df

⁵⁸ Nie, Z.; Long, R.; Teguh, J. S.; Huang, C.-C.; Hewak, D. W.; Yeow, E. K. L.; Shen, Z.; Prezhdo, O. V.; Loh, Z.-H. Ultrafast Electron and Hole Relaxation Pathways in Few-Layer MoS₂. *J. Phys. Chem. C* **2015**, *119*, 20698–20708. DOI: 10.1021/acs.jpcc.5b05048

⁵⁹ Völzer, T.; Fennel, F.; Korn, T.; Lochbrunner, S. Fluence-Dependent Dynamics of Localized Excited Species in Monolayer versus Bulk MoS₂. *Phys. Rev. B* **2021**, *103*, 045423. DOI: 10.1103/PhysRevB.103.045423

⁶⁰ Herman, A. P.; Zelewski, S. J.; Misztal, K.; Kudrawiec, R. Probing the Long-Lived Photo-Generated Charge Carriers in Transition Metal Dichalcogenides by Time-Resolved Microwave Photoconductivity. *Nanophotonics* **2022**, *11*, 1335–1344. DOI: 10.1515/nanoph-2021-0741

⁶¹ Li, Y.; Xu, C.-Y.; Wang, J.; Zhen, L. Photodiode-Like Behavior and Excellent Photoresponse of Vertical Si/Monolayer MoS₂ Heterostructures. *Sci. Rep.* **2014**, *4*, 7186. DOI: 10.1038/srep07186

⁶² Fan, Y.; Zhou, Y.; Wang, X.; Tan, H.; Rong, Y.; Warner, J. H. Photoinduced Schottky Barrier Lowering in 2D Monolayer WS₂ Photodetectors. *Adv. Opt. Mater.* **2016**, *4*, 1573–1581. DOI: 10.1002/adom.201600221

⁶³ Hamers, R. J.; Cahill, D. G. Ultrafast Time Resolution in Scanned Probe Microscopies: Surface Photovoltage on Si(111)-(7×7). *J. Vac. Sci. Technol. B* **1991**, *9*, 514–518. DOI: 10.1116/1.585559

⁶⁴ Yoshida, S.; Terada, Y.; Yokota, M.; Takeuchi, O.; Mera, Y.; Shigekawa, H. Direct Probing of Transient Photocurrent Dynamics in p-WSe₂ by Time-Resolved Scanning Tunneling Microscopy. *Appl. Phys. Express* **2013**, *6*, 016601. DOI: 10.7567/APEX.6.016601

⁶⁵ Yoshida, S.; Kanitani, Y.; Takeuchi, O.; Shigekawa, H. Probing Nanoscale Potential Modulation by Defect-Induced Gap States on GaAs(110) with Light-Modulated Scanning Tunneling Spectroscopy. *Appl. Phys. Lett.* **2008**, *92*, 102105. DOI: 10.1063/1.2888733

⁶⁶ Shockley, W.; Read, W. T., Jr. Statistics of the Recombinations of Holes and Electrons. *Phys. Rev.* **1952**, *87*, 835–842. DOI: 10.1103/PhysRev.87.835

⁶⁷ Hall, R. N. Germanium rectifier characteristics. *Phys Rev.* **1951**, *83*, 228.

⁶⁸ Liraz, D.; Cheng, P.; Yang, Y.; Tessler, N. Light-Induced Trap Emptying Revealed by Intensity-Dependent Quantum Efficiency of Organic Solar Cells. *J. Appl. Phys.* **2022**, *131*, 135501. DOI: 10.1063/5.0084184

⁶⁹ Kumar, J.; Shrivastava, M. Role of Chalcogen Defect Introducing Metal-Induced Gap States and Its Implications for Metal–TMDs’ Interface Chemistry. *ACS Omega* **2023**, *8*, 10176–10184.

DOI: 10.1021/acsomega.2c07489

⁷⁰ Mogi, H.; Wang, Z.-h.; Kikuchi, R.; Yoon, C. H.; Yoshida, S.; Takeuchi, O.; Shigekawa, H. Externally Triggerable Optical Pump-Probe Scanning Tunneling Microscopy. *Appl. Phys. Express* **2019**, *12*, 025005. DOI: 10.7567/1882-0786/aaf8b2

⁷¹ Iwaya, K.; Yokota, M.; Hanada, H.; Mogi, H.; Yoshida, S.; Takeuchi, O.; Miyatake, Y.; Shigekawa, H. Externally-Triggerable Optical Pump-Probe Scanning Tunneling Microscopy with a Time Resolution of Tens-Picoseconds. *Sci. Rep.* **2023**, *13*, 818. DOI: 10.1038/s41598-023-27383-z

Supporting Information

Concerted Carrier-Barrier Dynamics in van der Waals Schottky Junctions Revealed by Time-Resolved Atomic Force Microscopy

Munenori Yokota^{1‡}, Hiroyuki Mogi^{2‡}, Yutaka Mera³, Katsuya Iwaya^{1*}, Taketoshi Minato^{4,5}, Shoji Yoshida², Osamu Takeuchi², Tatsuo Nakagawa¹, and Hidemi Shigekawa^{2*}

¹ UNISOKU Co., Ltd., Osaka 573-0131, Japan.

² Faculty of Pure and Applied Sciences, University of Tsukuba, Ibaraki 305-8573, Japan.

³ Department of Fundamental Biosciences (Physics), Shiga University of Medical Science, Shiga 520-2192, Japan.

⁴ Institute for Molecular Science (IMS), National Institutes of Natural Sciences, Aichi 444-8585, Japan.

⁵ Core for Spin Life Sciences, Okazaki Collaborative Platform, National Institutes of Natural Sciences, Okazaki, Aichi 444-8585, Japan.

[‡] These authors contributed equally.

1. Picosecond-to-Microsecond Transient Absorption Spectroscopy (ps-TAS): Randomly Interleaved Pulse Train (RIPT) Method

In conventional pump–probe spectroscopy, ultrafast processes in the femtosecond–picosecond regime can be measured with high temporal resolution. However, because the pump–probe delay must be controlled through differences in optical path length, the accessible delay range is typically limited to only a few nanoseconds. Extending the delay into the tens-of-nanoseconds regime requires translating the optical delay stage over distances of a few meters, which poses significant challenges in terms of mechanical stability and measurement efficiency. As a result, time delays longer than several nanoseconds are effectively difficult to access.

On the other hand, nanosecond flash photolysis—using relatively long pulses from xenon lamps or nanosecond lasers—can probe dynamics up to the millisecond regime, but its temporal resolution is limited by the detector response time (typically several to tens of nanoseconds). Consequently, the 1–tens of nanoseconds window has traditionally been a “blind gap” in time-resolved spectroscopy (Fig. S1a).

The RIPT method addresses this temporal gap by operating the pump and probe beams with picosecond pulse widths independently, without synchronizing their repetition rates, and exploiting the naturally occurring asynchronous timing to generate random pump–probe delays¹. As illustrated in Fig. S1b, the sample is first excited by a pump pulse (e.g., 1 kHz, 50 ps), after which a sequence of probe pulses (e.g., 20 MHz, 100 ps) continuously monitors the transmitted signal. Because the arrival time of each probe pulse at the sample varies relative to each pump excitation, a wide range of delay times t_d is automatically produced (upper panel of Fig. S1c). By precisely determining the delay associated with each excitation—using a fast photodiode signal—and plotting the corresponding transient transmission intensity $I(t_d)$, we can reconstruct a broad delay-time window without any mechanical scanning of the optical path (lower panel of Fig. S1c).

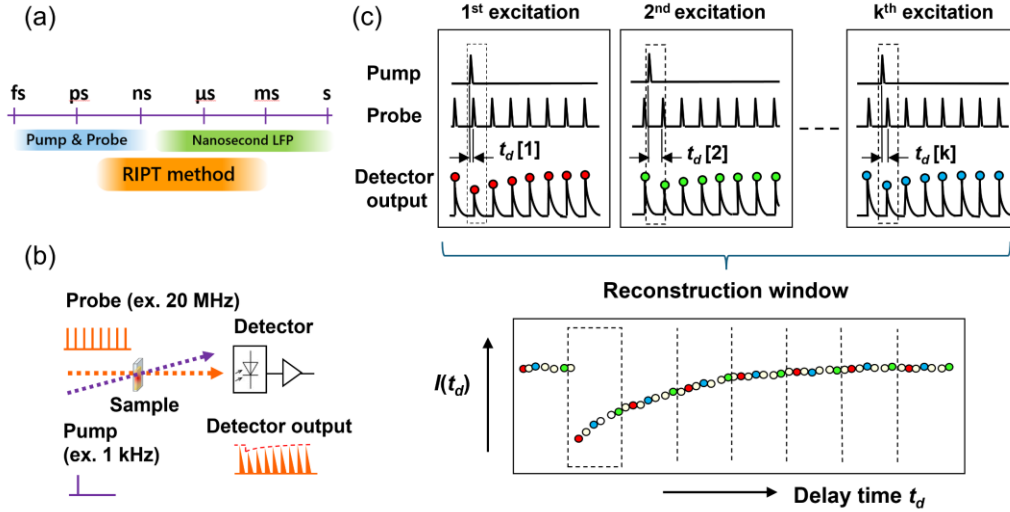


Figure S1. (a) Time ranges accessible with different transient absorption spectroscopy techniques. Femtosecond–picosecond dynamics can be measured by conventional pump–probe spectroscopy, while nanosecond flash photolysis (LFP) covers delays beyond several tens of nanoseconds. The RIPT method continuously bridges the intermediate “blind-gap” region. (b) Basic configuration of the RIPT method. The sample is excited by picosecond pump pulses, and absorption changes are detected by a high-repetition-rate picosecond probe pulse train operating asynchronously. The relative timing between the pump and probe pulses varies shot by shot and is passively measured. (c) Timing relationship between pump and probe pulses for each excitation shot. By extracting the absorption change at each delay time $t_d[k]$ from the corresponding probe signal and combining all data points, a transient absorption curve spanning a wide delay-time window from the picosecond to microsecond regime can be reconstructed.

2. Transient Absorption Spectroscopy of Bulk WSe₂

To first clarify the photoexcited states in bulk WSe₂, we measured the UV–visible absorption spectrum. As shown in the top panel of Fig. S2a, three optical transitions were identified at 470 nm (2.6 eV), 560 nm (2.2 eV), and 760 nm (1.6 eV). The peaks at 760 nm and 560 nm correspond to the A and B transitions, arising from direct excitation from the two spin–orbit–split valence-band states at the K point V1 and V2 to the conduction-band minimum C1 (Fig. S2b). In bulk WSe₂, the exciton binding energy is

relatively small (~ 30 meV), comparable to the thermal energy at room temperature, and prior studies have shown that photoexcitation in this regime predominantly leads to free-carrier generation on the picosecond timescale².

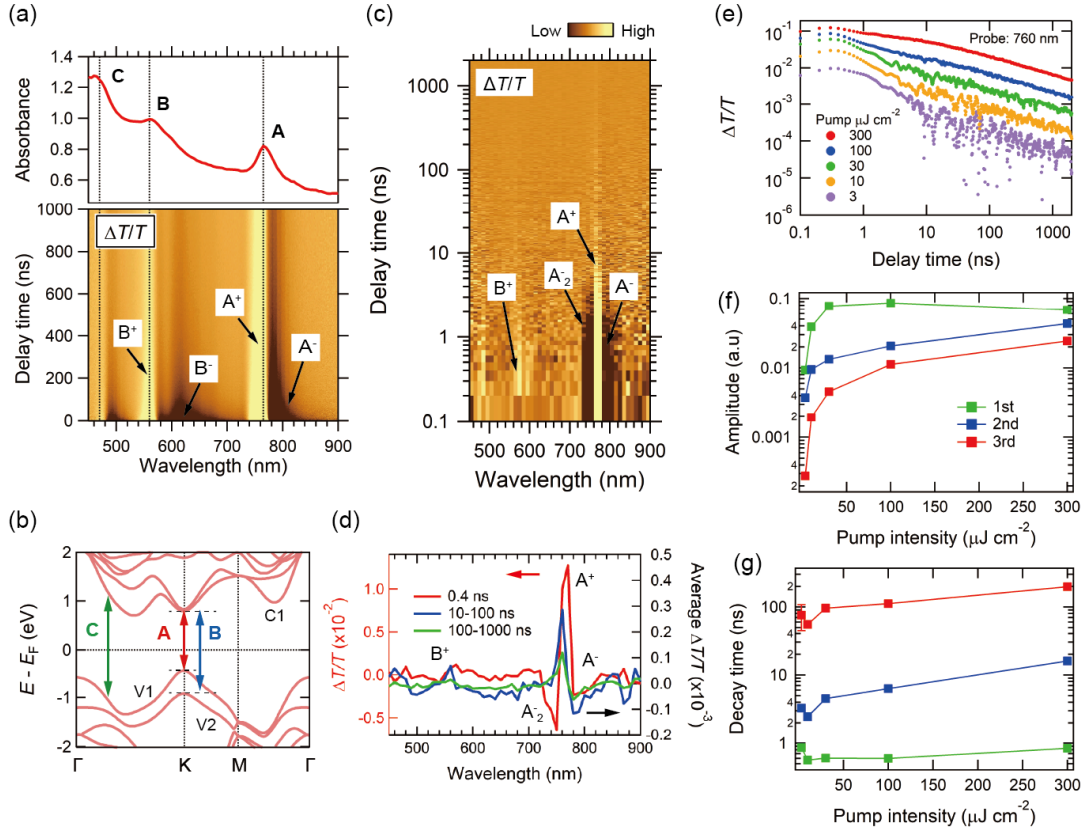


Figure S2. (a) (Top) Steady-state absorption spectrum of bulk WSe₂ at room temperature. (Bottom) Delay-time dependence of the differential transmission $\Delta T/T$ measured using the RIPT method. Pump wavelength: 480 nm; pump fluence: 300 $\mu\text{J cm}^{-2}$. The probe intensity is approximately 10^{-3} of the pump. The characteristic spectral features are assigned to A⁺, A⁻, B⁺, and B⁻. The line profiles at delay times of 0.5, 1, 10, and 100 ns are shown in Fig. 1e of the main text. (b) Band dispersion of bulk WSe₂. The peaks near 760 nm and 560 nm in (a) correspond to interband transitions from the valence-band states V1 and V2 at the K point to the conduction-band minimum C1 (A and B absorption edges). The C transition at ~ 470 nm corresponds to a higher-energy interband transition. (c) Delay-time dependence of $\Delta T/T$ at a pump fluence of 3 $\mu\text{J cm}^{-2}$, comparable to that used in the OPP-TR-AFM measurements. The spectral features are assigned to A⁺, A⁻, A₂⁻, and B⁺. (d) Transient absorption spectra at representative delay regions from (c): 0.4 ns, the 10–100 ns average, and the 100–1000 ns average. (e) Delay-time dependence of $\Delta T/T$ at 760 nm for various pump fluences. (f, g) Amplitudes (f) and decay times (g) extracted from tri-exponential fits to the curves in (e). At the pump fluence of 3 $\mu\text{J cm}^{-2}$, the decay times obtained are 0.9 ns, 3.3 ns, and 75.9 ± 30 ns.

To investigate the dynamics of these photoexcited carriers after relaxation to the conduction-band minimum, we performed ps-TAS using the RIPT method (picoTAS, Unisoku), covering the sub-nanosecond to microsecond range. Figure S2c shows the delay-time dependence of the differential transmission $\Delta T/T$, measured under pump fluence conditions comparable to those used in the OPP-TR-AFM experiments. Excited-state features near the A absorption edge (A^+ , A^- , A_2) and the B-edge component (B^+) are clearly resolved.

The A^+ feature persists over a wide temporal range (0.1–1000 ns), as also seen in the $\Delta T/T$ spectra extracted at selected delays (0.4 ns, 10–100 ns, and 100–1000 ns) in Fig. S2d. Figure S2e shows the delay-time dependence of $\Delta T/T$ at 760 nm measured under various pump fluences. In particular, for the $\Delta T/T$ signal obtained at a pump fluence of $3 \mu\text{J cm}^{-2}$, which is nearly identical to that used in the OPP-TR-AFM measurements, the decay dynamics were well reproduced by a tri-exponential fit, yielding decay constants of 0.9 ns, 3.8 ns, and 75.9 ± 30 ns. Previous time-resolved microwave conductivity studies have attributed the nanosecond component to trapping of free electrons into defect states, while the ~ 100 -ns component corresponds to recombination between trapped electrons and valence-band holes³.

3. Theoretical Simulations

When considering the time-resolved current flowing through a Schottky junction under optical excitation, the total current can be decomposed into four contributions as schematically illustrated in Fig. 3a-iv of the main text. In the present experiments, the optical pulses were incident not on the Schottky electrode surface but from the backside of the WSe₂ sample, which is relatively thick (several micrometers) and opaque to the excitation wavelength. Consequently, current contributions arising from direct photoexcitation of the depletion region or the metal electrode are expected to be negligibly small and to decay rapidly. As discussed in the main text, the characteristic bias-voltage and excitation-intensity dependences of the time-resolved current observed in the bias region of interest ($-0.3 \text{ V} < V_s < +1.5 \text{ V}$) can therefore be primarily attributed to the thermionic current, I_{th} , and the hole-diffusion current, I_{hole} . Each current component is described in detail below.

(1) Thermionic current

The thermionic current I_{th} is present even in the absence of photoexcitation and can be expressed as⁴

$$I_{\text{th}} = \exp\left(\frac{qV_{\text{is}}(t)}{kT}\right) \cdot I_{\text{dark}} = \exp\left(\frac{qV_{\text{is}}(t)}{kT}\right) \cdot I_0 \cdot \left(\exp\left(-\frac{qV_{\text{R}}}{nkT}\right) - 1\right)$$

$$= AA^*T^2 \exp\left(-\frac{q(V_{\text{sb}} - V_{\text{is}}(t))}{kT}\right) \cdot \left(\exp\left(-\frac{qV_{\text{R}}}{nkT}\right) - 1\right) \quad (\text{S1})$$

where q is the elementary charge; $V_{\text{is}}(t)$ is the potential drop associated with the occupation of interfacial trap states (see Eq. S4); k is the Boltzmann constant; T is the absolute temperature; V_{R} is the externally applied reverse bias; n is the ideality factor of the Schottky junction; I_{dark} is the dark current; I_0 is the reverse saturation current; A is the junction area; A^* is the effective Richardson constant; and V_{sb} is the Schottky barrier height. For clarity, the reverse-bias voltage V_{R} corresponds to the positive sample bias voltage V_{s} applied in the OPP-TR-AFM measurements.

(2) Hole current

The hole current flows when photo-generated holes reach the metal–semiconductor interface. This contribution consists of two components:

- I_{hole1} : holes generated within the depletion region by the pump pulse, which are rapidly driven to the interface by the built-in electric field. This contribution is expected to be negligibly small and to decay rapidly under the present experimental conditions, and is therefore neglected in the analysis.
- I_{hole2} : holes generated in the semiconductor bulk that subsequently diffuse into the depletion region and reach the interface before recombining. This component corresponds to I_{hole} in the main text.

The two components are expressed as

$$I_{\text{hole1}} = \frac{qP}{h\nu} \cdot \eta_{\text{qe}} \cdot \frac{w}{d_{\text{s}}} \cdot \Lambda_2 \quad (\text{S2})$$

$$I_{\text{hole2}} = qN_{\text{p}}(t) \cdot \Lambda_3 \quad (\text{S3})$$

Here, η_{qe} is the quantum efficiency in the semiconductor; w is the depletion layer width; d_{s} is the thickness of the semiconductor sample; Λ_2 is a fitting parameter. $N_{\text{p}}(t)$ is the hole concentration in the bulk; and Λ_3 is a fitting parameter that incorporates the effects of hole diffusion in the bulk as well as trapping processes at the interface.

In addition, the Schottky interface hosts trap states that capture photo-generated holes. When holes arriving at the interface are trapped in these interface states, the resulting charge modifies the effective Schottky barrier height ($V_{\text{sb}} - V_{\text{is}}$).

As seen in Eq. S1, the thermionic current I_{th} is sensitive to changes in the effective barrier height. We assume that the change in the Schottky barrier, V_{is} , depends logarithmically on the hole population N_{is} in

the interface states⁵, following

$$V_{is} = V_{is0} \cdot \ln \left(1 + \alpha \frac{N_{is}(t)}{N_{\text{dark}}} \right) \quad (\text{S4})$$

Here, V_{is0} is a parameter that sets the magnitude of V_{is} ; α is a parameter describing how holes trapped at surface states reduce the effective Schottky barrier height; and N_{dark} is the electron concentration under dark conditions.

The hole-diffusion current I_{hole2} supplies holes to the interfacial trap states. Once holes are trapped, their concentration decreases as electrons tunnel into the interface states; the rate of this decrease depends on the rate of electrons arriving at the interface. Consequently, bias-induced modulation of the effective barrier height is expected to affect the temporal decay of hole populations in the interfacial trap states. Based on this consideration, the relaxation time τ_{is} associated with the decrease in hole population at the interfacial trap states was modeled as

$$\tau_{is} = \tau_{is0} \cdot (1 - \beta V_R) \quad (\text{S5})$$

such that the relaxation time decreases linearly with the applied reverse bias V_R . Here, τ_{is0} is τ_{is} at zero bias, and β is a parameter that describes the reduction of τ_{is} with increasing reverse bias. Here, $N_{is} \propto \exp(-t/\tau_{is})$, which, via V_{is} (Eq. S4), affects the thermionic current I_{th} (Eq. S1).

The hole current arising from carriers that diffuse from the bulk WSe₂ is proportional to the local hole density, which itself relaxes through recombination with electrons. As discussed in the main text, the recombination rate τ_p is influenced by recombination centers within the bandgap and therefore depends on the instantaneous hole density (main text Fig. 4e). This dependence is well described by the following equation:

$$\tau_p = \tau_{p_base} + \tau_{p_base} \cdot \frac{1}{1 + \frac{N_{\text{dark}}}{N_p(t)}} \quad (\text{S6})$$

where τ_{p_base} is the recombination lifetime at low hole concentrations.

For example, a longer τ_p corresponds to a slower depletion of bulk holes. Consequently, the hole current I_{hole2} (Eq. S3) persists for a longer duration, continuously supplying holes to the interfacial trap states. This, in turn, affects the interfacial state population N_{is} and the associated Schottky barrier modulation V_{is} , leading to changes in the thermionic current I_{th} .

Under these conditions, each current component was calculated at a given delay time $t_d = t_D$, and the time-resolved current $I_L(t_D)$ was obtained using Eq. (1) in the main text. In addition, for high excitation intensities, the calculations were performed under the condition that nearly all interfacial states are occupied by trapped holes.

-
- ¹ Nakagawa, T., Okamoto, K., Hanada, H., & Katoh, R. Probing with randomly interleaved pulse train bridges the gap between ultrafast pump-probe and nanosecond flash photolysis. *Opt. Lett.* **41**, 1498-1501 (2016).
- ² Völzer, T., Lütgens, M., Fennel, F., & Lochbrunner, S. Recombination Dynamics of Optically Excited Charge Carriers in Bulk MoS₂. *J. Phys. B: At. Mol. Opt. Phys.* **50**, 194003 (2017).
- ³ Herman, A. P. et al. Probing the long-lived photo-generated charge carriers in transition metal dichalcogenides by time-resolved microwave photoconductivity. *Nanophotonics* **11**, 1335-1344 (2022).
- ⁴ Atalla, M. R. M. et al. Modeling the spectral responsivity of ultraviolet GaN Schottky barrier photodetectors under reverse bias. *J. Appl. Phys.* **117**, 134503 (2015).
- ⁵ Hamers, R. J., & Cahill, D. G. Ultrafast time resolution in scanned probe microscopies: Surface photovoltage on Si(111)-(7×7). *J. Vac. Sci. Technol. B* **9**, 514-518 (1991).